Optimal mixing in recirculation zones

Bernd R. Noack[a)]
Hermann-Föttinger-Institut für Strömungsmechanik, Technische Universität Berlin, Strasse des 17. Juni 135, D-10623 Berlin, Germany

Igor Mezić[b)]
Department of Mechanical and Environmental Engineering and Department of Mathematics, University of California, Santa Barbara, California 93106-5070

Gilead Tadmor[c)]
Department of Electrical and Computer Engineering, Northeastern University, Boston, Massachusetts 02115

Andrzej Banaszuk[d)]
United Technologies Research Center, East Hartford, Connecticut 06108

(Received 18 March 2003; accepted 9 December 2003; published online 13 February 2004)

Coarse-scale mixing in a recirculation zone is described with a simple vortex model. Time-dependent forcing is employed to change the vortex motion and mixing properties. An optimal mixing problem is defined in which the flux across the recirculation region shall be maximized under the side-constraints of bounded vortex motion and bounded actuation. Concepts of control theory and chaotic advection are used to achieve this goal. In particular, controllability is proven with a transformation into flat coordinates. Thus, a feedforward law for the optimal trajectory and a feedback law for its stabilization are derived. Observability of the vortex motion is indicated by a dynamic observer. Mixing in the optimized flow is studied using Poincaré maps. The low-frequency modulations to vortex motion are shown to substantially increase mixing in the average. Generalizations of the mathematical framework for mixing optimization are suggested for a larger class of models and flows. © *2004 American Institute of Physics.*
[DOI: 10.1063/1.1645276]

I. INTRODUCTION

Hydrodynamic mixing is an important aspect of many flow control applications. A major motivation of flow control is to increase the performance of flow machines with small associated actuation penalties. The performance may be related to drag reduction, to an increase of lift, to mixing enhancement, or to noise reduction. For turbulent flow, the performance benefits are strongly correlated with mixing enhancement or mixing reduction in free or wall-bounded shear-layers.[1,2]

The effect of hydrodynamic fluctuations and mixing on the mean flow has been subject of intensive study for more than 100 years since the Boussinesq ansatz (1887) and the Reynolds decomposition (1895) (see, for instance, Refs. 3 and 4). Statistical fluid mechanics provides also effective models of fluid-particle mixing based on the inertial range of the Kolmogorov cascade, e.g., Richardson's theory with spectral eddy diffusivities (see also Refs. 3 and 4).

The characterization of large-scale mixing associated with coherent turbulent structures and with laminar unsteady flow has become subject of increasing research since the last two decades. In particular, dynamical systems theory has proven as a powerful method.[5–11] Typically, emphasis is placed on *understanding the mechanisms* of mixing in laminar flows. For example, Melnikov theory and associated lobe dynamics is used to study transport and mixing across the recirculation bubble of the Batchelor's vortex pair in a pioneering study of Rom-Kedar, Leonard, and Wiggins.[12] Recent results in this direction include extension of dynamical systems ideas to aperiodic flows.[9,13–15]

In contrast, in the current study, a problem of mixing *control and optimization* is posed in the framework of low-dimensional point-vortex models, dynamical systems theory, and control theory. As the dynamics of point vortices can be described using a finite-dimensional (Hamiltonian) system of ordinary differential equations (see, for instance, Ref. 16). Methods of the control theory can be used to achieve various control objectives like stabilization of vortex configurations,[17,18] enhancement of mixing,[19,21] and improvement of airfoil lift.[22] Early studies by Cortelezzi and co-workers in this direction are based mostly on modeling and reduced-order numerical simulations using vortex elements (see Refs. 23 and 24 and the references therein). The numerical approaches have also been coupled to control theory utilizing mostly linear control theory concepts for the purpose of stabilization. By now there is a large amount of literature on this topic.[18,25]

Here, however, our focus is *destabilization and mixing* of fluid particle motion. Our approach consists of the following steps. Fluid flow is described by a finite-dimensional

[a)]Electronic mail: noackbr@pi.tu-berlin.de
[b)]Electronic mail: mezic@engineering.ucsb.edu
[c)]Electronic mail: tadmor@ece.neu.edu
[d)]Electronic mail: banasza@utrc.utc.com

model using point vortices. An optimal control problem is posed with a mixing objective, namely flux through a distinguished curve. We identify the optimal vortex motion for that objective. Then, optimal vortex motion is stabilized with an observer and a feedback law. This approach is in spirit similar to that taken in Ref. 19. A feedback-control approach to this question can be found in Refs. 26 and 27. In the appendix, the control approach of the main body is extended to N vortices. In particular, sufficient conditions for controllability for this system are provided.

This paper is organized as follows: In Sec. II, the point-vortex idealization of the recirculation zone is presented. In Sec. III, the natural, forced, and controlled vortex dynamics are described. In Sec. IV, the mixing associated with natural vortex motion is characterized based on fluid particle motion and Poincaré maps. In Sec. V, an optimum mixing problem for control is posed and solved. Thus, the achievable changes of flux and residence times are elucidated. In Sec. VI, the flux is compared with other mixing measures proposed in the literature. The main conclusions and an outlook is presented in Sec. VIII.

II. THE POINT-VORTEX MODEL

In this section, the vortex model for the recirculation region is outlined generalizing an analytical study of unforced flow by Shu.[28]

The flow is described in a Cartesian coordinate system x,y of which the origin coincides with the corner. The walls of the corner lie on the x and y axes and the considered domain is the first quadrant $\mathcal{Q}_I := \{(x,y): x \geqslant 0,\ y \geqslant 0\}$. The independent variables are the location $\mathbf{x} := (x,y)$ and the time t. The x and y components of the fluid velocity $\mathbf{u}$ are denoted by u and v, respectively.

The potential corner flow is expressed by the stream function

$$\Psi_0(\mathbf{x}) = k\ x\ y, \tag{1}$$

or, equivalently, the velocity field $u = \partial_y \Psi_0 = k\,x$, $v = -\partial_x \Psi_0 = -k\,y$. The constant k specifies the magnitude of the velocity at a given location. Figure 1 (top) shows the corresponding streamlines. The corner flow can be considered as one quadrant of a saddle point.

A vortex with circulation $-\Gamma$, where $\Gamma > 0$, is placed at $\mathbf{x}_v = (x_v, y_v)$. The negative sign of the circulation indicates that the induced fluid motion rotates in a clockwise direction. The no-penetration condition at the walls is enforced by mirror vortices in quadrants 2, 3, and 4 at $\mathbf{x}_2 = (-x_v, y_v)$, at $\mathbf{x}_3 = (-x_v, -y_v)$, and at $\mathbf{x}_4 = (x_v, -y_v)$, respectively. The circulation of the mirror vortex in quadrant n is given by $\Gamma_n = (-1)^n\,\Gamma$. For reasons of simplicity, the position of vortex in the domain $\mathcal{Q}_I$ is denoted by $\mathbf{x}_1 = \mathbf{x}_v$ and the circulation by $\Gamma_1 = -\Gamma$ in the sequel.

The stream function induced by the four vortices at location $\mathbf{x}$ is given by

$$\Psi_v(\mathbf{x}) = \sum_{n=1}^{4} \frac{\Gamma_n}{2\pi} \ln \|\mathbf{x} - \mathbf{x}_n\|, \tag{2}$$

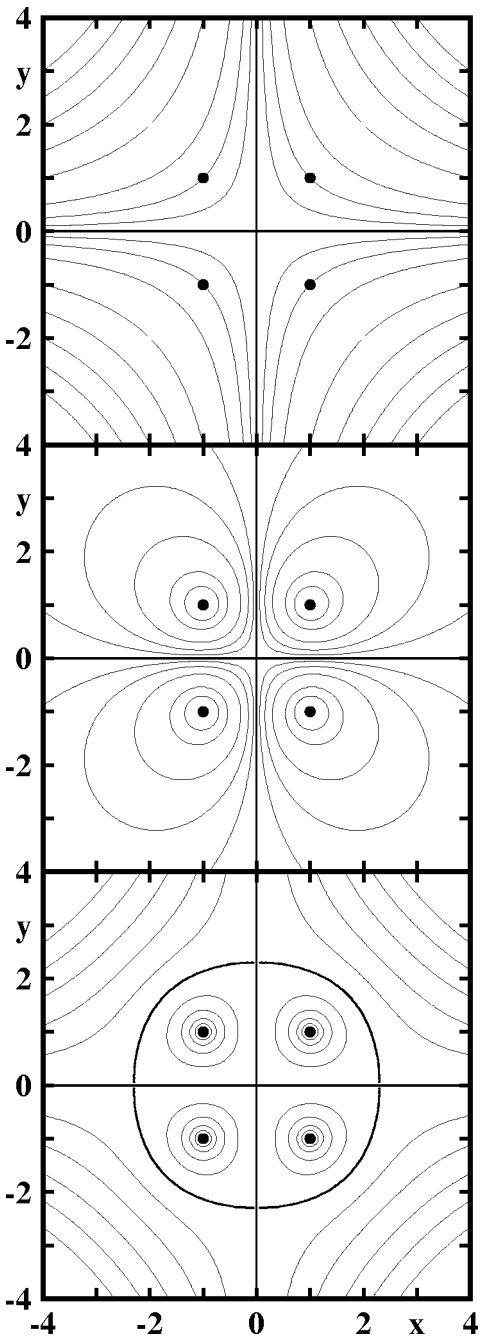

FIG. 1. Streamlines for the saddle point (top), the four vortices (middle), and the resulting flow (bottom). The four vortices are indicated by solid circles.

where $\|\mathbf{x} - \mathbf{x}_n\|$ represents the Euclidean distance between the location $\mathbf{x}$ and the nth vortex. Figure 1 (middle) illustrates the quadrupolelike streamlines of the induced velocity field. The stream function can be considered as a function of the location $\mathbf{x}$ and of the vortex position $\mathbf{x}_v$, since the positions of all mirror vortices are slaved to the real vortex at each instant. At the singularity $\mathbf{x} = \mathbf{x}_v$, Eq. (2) is not valid, since the real vortex does not experience a self-induction. The motion of the real vortex is determined by the potential corner flow and the velocity field induced by the mirror vortices. The stream function associated with the mirror vortices at the location $\mathbf{x}$ is given by

$$\Psi_{\mathrm{mv}}(\mathbf{x}) = \sum_{n=2}^{4} \frac{\Gamma_n}{2\pi} \ln \|\mathbf{x} - \mathbf{x}_n\|. \tag{3}$$

This stream function describes the effective field for the vortex at $\mathbf{x} = \mathbf{x}_1$ and is immaterial for other fluid particles.

Actuation is provided by the free-stream perturbation $a\ \Psi_a$, where a represents the time-dependent forcing amplitude and Ψ_a the free stream,

$$\Psi_a = \Psi_0 = kxy. \tag{4}$$

The stream function Ψ of the actuated recirculation zone contains the contribution of the potential corner flow, the actuation, and vortices,

$$\Psi = \Psi_0 + a\Psi_a + \Psi_v \tag{5}$$

or, employing Eqs. (1), (2), and (4),

$$\Psi = (1+a)kxy + \sum_{n=1}^{4} \frac{\Gamma_n}{2\pi} \ln \|\mathbf{x} - \mathbf{x}_n\|.$$

Figure 1 (bottom) illustrates the streamlines of this equation at the equilibrium vortex position under vanishing actuation, $a = 0$. At the vortex position $\mathbf{x} = \mathbf{x}_v$, the velocity field due to the real vortex must be discarded, i.e., Ψ_v, of Eq. (2) is replaced by Ψ_{mv} of Eq. (3).

The evolution equation for the vortex position is given by

$$\dot{\mathbf{x}}_v = \mathbf{f}(\mathbf{x}_v) + a\mathbf{g}(\mathbf{x}_v) \tag{6}$$

and contains the velocity field due to the natural dynamics $\mathbf{f} := (\partial_y[\Psi_0 + \Psi_{\mathrm{mv}}], -\partial_x[\Psi_0 + \Psi_{\mathrm{mv}}])|_{\mathbf{x}=\mathbf{x}_v}$ and the actuation field $\mathbf{g} := (\partial_y \Psi_a, -\partial_x \Psi_a)|_{\mathbf{x}=\mathbf{x}_v}$. At $a \equiv 0$, the evolution equation has the form of an autonomous system. Otherwise, time dependence due to a enters in a simple form which is well investigated in control theory.

In the following, all quantities are assumed to be nondimensionalized with length scale $L = \sqrt{\Gamma/8\pi k}$ and time scale $T = 1/2k$. The original symbols are used for reasons of simplicity. Thus, employing Eqs. (1), (3), (6) yields

$$\dot{x}_v = \frac{1}{2}(1+a)x_v - \frac{1}{y_v} + \frac{y_v}{r_v^2}, \tag{7a}$$

$$\dot{y}_v = -\frac{1}{2}(1+a)y_v + \frac{1}{x_v} - \frac{x_v}{r_v^2}, \tag{7b}$$

where $r_v := \sqrt{x_v^2 + y_v^2}$. Note that at $a \equiv 0$, the stream function (or Hamiltonian) for the velocity field (7) is given by

$$\Psi = \frac{x_v y_v}{2} + \ln\left(\frac{x_v}{y_v}\right) + \ln \sqrt{(x_v^2 + y_v^2)}. \tag{8}$$

The dynamics of the fluid is parametrized by the motion of the vortex. The motion of a fluid particle with position $\mathbf{x}_p$ is given by

$$\dot{\mathbf{x}}_p = (\partial_y \Psi, -\partial_x \Psi)|_{\mathbf{x}=\mathbf{x}_p}, \tag{9}$$

where Ψ represents the stream function (5) with the considered actuation fields.

The point-vortex idealization of the velocity field mimics the main properties of the real fluid mixing problem. By real we mean that the control a enters in the vortex motion equation (7) in the way it would enter into Navier–Stokes equation. On the other hand, we are primarily interested in changing the mixing properties of the flow (5), not the vortex dynamics (7). The control affects (5) both directly through the input a and indirectly, by changing the original velocity field as the position of the vortex has changed.

III. VORTEX MOTION

In this section, the vortex motion described in Sec. II is considered, partially following the work of Shu.[28] In Sec. III A, the equilibrium position of the vortex in a steady strain field is identified and its stability is discussed. In Sec. III B, periodic orbits of the unforced motion are described. In Sec. III C, the effect of periodic forcing is analyzed. Finally, controllability of vortex motion is studied in Sec. III D.

A. The fixed point

The vortex position $\mathbf{x}_{v0} = (x_{v0}, y_{v0}) = (1,1)$ is readily seen to be a fixed point of Eq. (7). At this point, the induced velocity of the mirror vortices is equal but opposite to the potential corner flow. No further fixed points exist in the domain $x_v, y_v > 0$ as can easily be analytically verified. In non-normalized coordinates, the fixed point is expressed by $x_{v0} = y_{v0} = \sqrt{\gamma/2k}$, i.e., the distance between the fixed point and the origin increases with the strength of the vortex and decreases with the magnitude of the potential corner flow, as intuitively plausible.

The dynamics of the infinitesimal perturbation $\mathbf{x}_v'$ around $\mathbf{x}_{v0}$ are described by

$$\dot{x}_v' = -y_v', \quad \dot{y}_v' = x_v'.$$

Hence, the fixed point is a center and small perturbations have angular frequency $\omega = 1$. The fixed point is marginally stable, i.e., an infinitesimal perturbation is neither exponentially amplified nor exponentially damped. The dimensional value of the frequency $\omega = 2k$ increases with potential flow magnitude and is independent of the circulation. A similar behavior of the fixed point and its small perturbations are observed by the authors for a single vortex in a more realistic backward-facing step configuration.[29]

B. Natural periodic motion

As shown in Sec. III A, the only critical point $(x_{v0}, y_{v0}) = (1,1)$ of the vortex dynamics is nonsingular. Trajectories close to the fixed point must be periodic orbits. In fact, all trajectories in the first quadrant of the plane (excluding the axis) have to be periodic orbits, since the topological type of the intersections of constant planes with the Hamiltonian (8) changes only at critical points. The velocity $\dot{x}_v$ can be zero only if $y_v \leqslant 1$ and $\dot{y}_v$ can be zero only if $x_v \leqslant 1$. These properties are reflected in numerical solutions of Eq. (7) shown in Fig. 2. The computed orbits are periodic trajectories around the fixed point with clockwise orientation.

The periodic behavior can also be made physically plausible. If the vortex is displaced from the equilibrium position away from the origin, the mirror vortices are too far away to

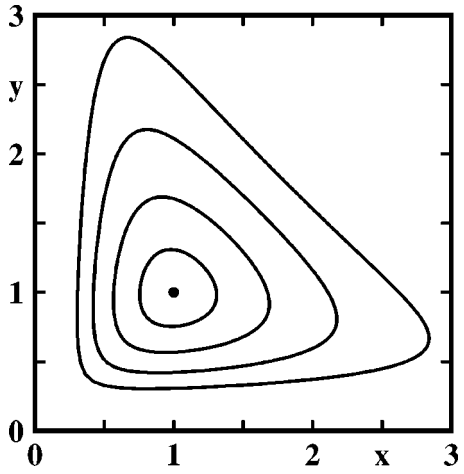

FIG. 2. Natural vortex motion of the point vortex in a strain field. The fixed point at (1,1) is indicated by a solid circle.

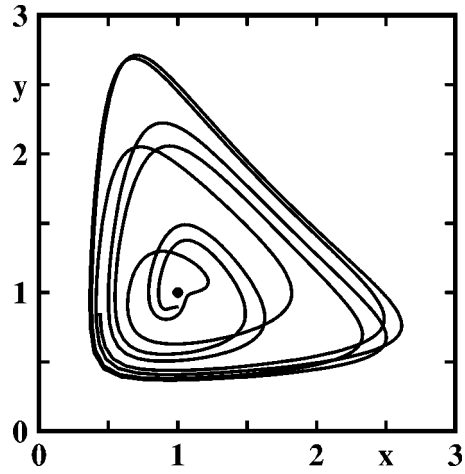

FIG. 4. Trajectory of periodically forced vortex motion with $a=0.2\sin(t)$. An infinitely long trajectory fills a nearly triangular region. The fixed point of natural vortex motion is indicated by a solid circle.

balance the potential flow and the vortex moves downstream with respect to the corner flow. The corner flow and the mirror vortex 2 supports a motion towards the wall $y=0$ where the vortex experiences the induced upstream velocity of mirror vortex 4. As the vortex returns below the streamline $\Psi_0=\Psi_0(1,1)$ through the fixed point, an upstream motion is induced by the mirror vortices 2 and 4. As the vortex moves in positive y direction, mirror vortex 4 induces a velocity component away from the wall and the vortex moves downstream above the $\Psi_p=\Psi(1,1)$ streamline, since the induced upstream field cannot be overcome by the increasing potential flow component $v=-ky$. Mirror vortex 3 weakens the induced velocity of the vortices 2 and 4 but is too far away to annihilate their effect.

The period T of the vortex motion is numerically observed to increase with the amplitude of oscillation (see Fig. 3). This amplitude is defined as the maximum distance of the orbit from the fixed point,

$$R:=\max_{\forall t}\|\mathbf{x}_v(t)-\mathbf{x}_{v0}\|. \tag{10}$$

C. Periodically forced vortex motion

In this section, the effect of time-periodic actuation is considered. From Sec. III B, the period of natural vortex motion T is found to increase with oscillation amplitude. In particular, at $R<0.5$, this relationship is approximately described by $T=2\pi\,(1+0.24R^2)$. This increase is a useful fact in considerations of forced vortex motion. In particular, consider time-periodic forcing with period $\tau=2\pi/\Omega$ and bounded by δ, i.e., $a(t)=a(t+\tau),|a|<\delta$. Then, most of the periodic orbits persist in the forced case for small enough δ. This persistence can be shown using Moser's version of the KAM theorem[30] and using the fact that $\partial T/\partial R>0$. In other words, the vortex motion will be periodic starting from most initial conditions if time-periodic forcing is small enough. Hence, vortex that starts at the equilibrium point will not drift far from it at any time, assuming again small time-periodic forcing, However, the motion of the vortex can become chaotic starting from some initial conditions. These initial conditions are close to resonant periodic orbits for which the period of unforced motion and the period of the forcing are rationally related.

Most numerically computed vortex motions with forcing frequency $\Omega=1$ seem to be nearly quasiperiodic with a dominant frequency near $\Omega=1$ and a beat frequency which scales with the inverse actuation amplitude $1/\delta$ (see Figs. 4 and 5).

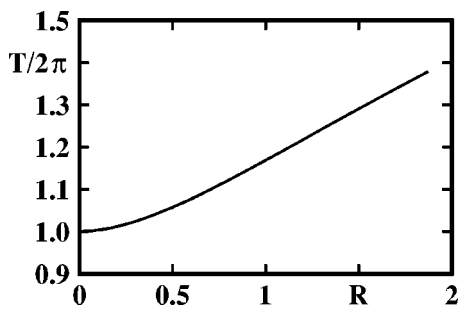

FIG. 3. Period T vs amplitude R of natural vortex motion (see Fig. 2).

D. Controlled motion

In this section, controllability of vortex motion is shown and control laws for the actuation amplitude a are derived.

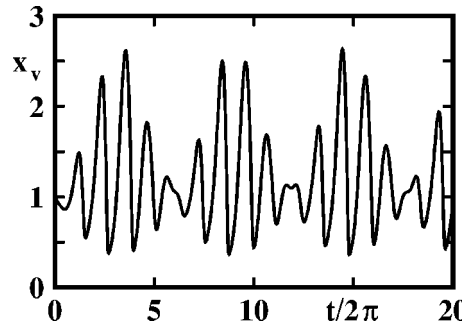

FIG. 5. Amplitude of periodically forced vortex motion with $a=0.2\sin(t)$. The x coordinate is shown as a function of time t.

In the pioneering mixing study of Rom-Kedar, Leonard, and Wiggins,[12] actuation of the vortex pair is assumed to be periodic. In the present study, we want to prescribe a much larger class of vortex motion by control laws for actuation as a function of time and vortex position, $a=a(x_v,y_v,t)$. This class includes periodic motion at arbitrary frequencies and at arbitrary not necessarily small amplitudes. The goal can be achieved in the framework of control theory.[31,32] The key element of the strategy is finding a transformation into the so-called flat coordinates

$$z_1=\alpha_1(x_v,y_v), \tag{11a}$$

$$z_2=\alpha_2(x_v,y_v), \tag{11b}$$

such that Eq. (7) can be expressed in the form

$$\dot{z}_1=z_2, \tag{12a}$$

$$\dot{z}_2=p(z_1,z_2)+a\ \ q(z_1,z_2). \tag{12b}$$

Thus, the first flat coordinate can be prescribed by an arbitrary function of time $z_1=z_1^d(t)$. The first derivative corresponds to the second flat coordinate $z_2^d=\dot{z}_1^d$. Equation (12) represents the controlled vortex dynamics and any such vortex motion (z_1^d,z_2^d) is easily seen to arise by imposing the control law

$$a=\frac{\dot{z}_2^d-p(z_1^d,z_2^d)}{q(z_1^d,z_2^d)}, \tag{13}$$

provided that $q\neq 0$.

Differentiation of the first coordinate (11a) and employing Eq. (6) yields

$$\dot{z}_1=L_f\alpha_1+aL_g\alpha_1 \tag{14}$$

with Lie derivatives $L_f\alpha_1:=f_1\ \partial_{x_v}\alpha_1+f_2\ \partial_{y_v}\alpha_1$ and $L_g\alpha_1:=g_1\ \partial_{x_v}\alpha_1+g_2\ \partial_{y_v}\alpha_1$. Comparing Eq. (14) with Eq. (12a) implies $L_g\alpha_1\equiv 0$ and $z_2=L_f\ \alpha_1$, since the first transformed equation (12a) does not contain a. Geometrically, the first condition requires that the gradient of the flat coordinate z_1 is everywhere perpendicular to the forcing field **g**, or, equivalently, that z_1 is a function of the stream function $\Psi_a=x_v\ y_v$.

Equation (7) can be brought into flat form by straightforward computations. The transformation is given by

$$z_1=x_v y_v, \tag{15a}$$

$$z_2=\frac{y_v^2-x_v^2}{r_v^2}, \tag{15b}$$

the inverse map being

$$x_v=\sqrt{z_1}\ \left(\frac{1-z_2}{1+z_2}\right)^{1/4}, \tag{16a}$$

$$y_v=\sqrt{z_1}\ \left(\frac{1+z_2}{1-z_2}\right)^{1/4}. \tag{16b}$$

Figure 6 illustrates the flat coordinates.

The dynamics in flat coordinates are described by

$$\dot{z}_1=z_2, \tag{17a}$$

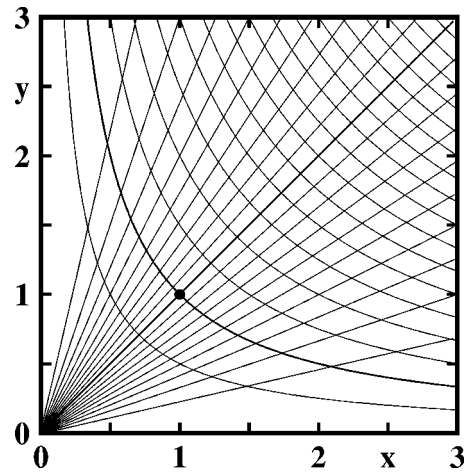

FIG. 6. Isolines of flat coordinates. The hyperbolae represent $z_1=0.5,1,1.5,\ldots,8.5$. The distance from the origin increases with the z_1 value. The rays represent $z_2=-0.9,-0.8,\ldots,0.9$. The angle from the x axis increases with the z_2 value. The intersection point of the lines $z_1=1$ and $z_2=0$ is the fixed point (1,1) (solid circle).

$$\dot{z}_2=p+aq, \tag{17b}$$

where $p=-4\,x_v\,y_v\,(x_v\,y_v-1)/r_v^4$ and $q=-4\,x_v^2\,y_v^2/r_v^4$. Hence, vortex motion is controllable. In other words, the vortex can be moved from an arbitrary point (z_{10},z_{20}) at time $t=0$ to another arbitrary point $(z_{1\tau},z_{2\tau})$ during the arbitrary time $t=\tau$ by prescribing a function $z_1^d(t)$ such that $z_1^d(0)=z_{10}$, $\dot{z}_1^d(0)=z_{20}$, and $z_1^d(\tau)=z_{1\tau}$, $\dot{z}_1^d(T)=z_{2T}$. Then, controllability follows by applying the control law (13), since q does not vanish in the domain $x_v,y_v>0$.

The control law (13) has to be enhanced by stabilizing feedback terms to account for transient behavior,

$$a=\frac{\dot{z}_2^d-p(z_1,z_2)-k_1(z_1-z_1^d)-k_2(z_2-z_2^d)}{q(z_1,z_2)}. \tag{18}$$

The coefficients k_1, k_2 must be chosen such that the deviations $e_1=z_1-z_1^d$, $e_2=z_2-z_2^d$ tend to zero with increasing time. The dynamics of the tracking error with the modified control law (18) can be derived from Eq. (17),

$$\dot{e}_1=e_2, \tag{19a}$$

$$\dot{e}_2=-k_1e_1-k_2e_2. \tag{19b}$$

A particular choice of feedback gains k_1 and k_2 that make the tracking errors e_1 and e_2 decay can be obtained as follows. Let $e_1=e^{-\lambda t}$, then Eq. (19a) implies $e_2=-\lambda\ e^{-\lambda t}$ and from Eq. (19b) the coefficients are given by $k_1=\lambda^2$ and $k_2=2\lambda$. In principle, the controlled vortex motion (17) and (18) can be analytically described by the inverse map (16) for the vortex position and the solution in terms of flat coordinates $z_n=z_n^d+e_n$, $n=1,2$. The inverse map can generally not be analytically expressed and the evolution equation (7) is solved numerically employing the control law (18) as a function of the flat coordinates $z_n=\alpha_n(x_v,y_v)$, $n=1,2$.

A generalization for N-vortex motion and more general actuation is proposed in Appendix A.

IV. NATURAL MIXING

In this section, mixing is analyzed for natural vortex motion with amplitude $R=0.5$. Without loss of generality, we assume in all results that the vortex crosses the $x=y$ axis in clockwise direction at time $t=0$. First (Sec. IV A), the topology of the flow field is briefly described. In Sec. IV B, the resulting fluid particle motion is classified. This motion is characterized in terms of the invariant manifolds of a Poincaré map (Sec. IV C). Finally (Sec. IV D), a measure for mixing is proposed based on the analysis of the preceding sections.

A. Flow field

Mixing is considered for natural vortex motion $(x_v(t),y_v(t))$ at amplitude $R=0.5$ [see Eq. (10)]. At all instants, the velocity field has three instantaneous stagnation (zero-velocity) points, one at the origin, one on the x axis, and another one on the y axis. The two time-dependent stagnation points on the x and the y axis are connected by a streamline, the so-called *instantaneous separatrix*. The separatrix is employed to define the *instantaneous recirculation zone* bounded by the x axis, the y axis, and the separatrix. In this recirculation zone, the streamlines are closed orbits containing the vortex in its interior. Outside the recirculation zone, the streamlines converge to the x and the y axis. The direction of the flow is everywhere in the clockwise direction with respect to the vortex. The topology of the flow field is the same as for the equilibrium position (see Fig. 1) at all instants. The circulation zone is numerically found to be stretched in the same direction as the vortex displacement. A detailed analysis of the flow field in dependence of the vortex position is given in Ref. 28.

B. Fluid particle motion

Under steady conditions, i.e., if the vortex is located at its equilibrium position (1,1), the pathlines of the fluid particles coincide with the streamlines. Under the considered periodic vortex motions, the fluid particle follows the streamline only locally at a given instant. Generally streamlines and pathlines are different.

A numerical study indicates that all fluid particles move around the vortex in clock-wise direction in alignment with the instantaneous velocity fields described in Sec. IV A. The fluid particles can be classified in dependency of the amount of revolutions L around the vortex following a similar suggestion of Ref. 12. This number of loops L is defined to be the number of intersections of the fluid particle path with the time-dependent ray (half-line) starting from the vortex with an inclination of 225°. In other words, the amount of revolutions is the amount of the events $x_p-x_v=y_p-y_v<0$. It should be borne in mind that the fluid particle passes through this ray always in clockwise direction around the vortex. The amount of revolutions is denoted by L^+, if the fluid particle is considered at all times $(t>0)$ and by L^- if the fluid particle is considered at $(t<0)$. L^0 shall be unity if $x_p-x_v=y_p-y_v<0$ at $t=0$ and vanishes otherwise. Evidently, $L^0=1$ on the $x_p=y_p\leqslant x_v(0)=y_v(0)\approx 1.301$ due to the assumed initial vortex position. The amount of revolutions during the complete history $-\infty<t<\infty$ is given by $L=L^+ +L^-+L^0$.

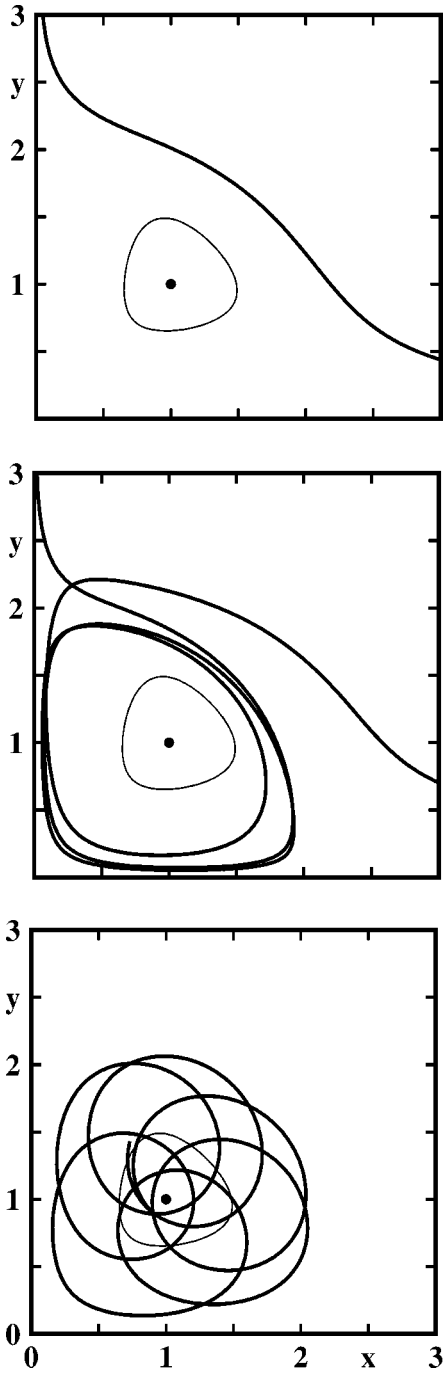

FIG. 7. Pathlines of free (top), mixing (middle), and trapped (bottom) fluid particle. The fixed point is indicated by a solid circle. The orbit of the vortex motion is illustrated by the thin closed curve.

If $L=0$ or $L=\infty$ the fluid particle is considered free or trapped, respectively. Otherwise, i.e., $0<L<\infty$, the mixing fluid particle revolves a finite amount of time around the vortex before it escapes. Figure 7 shows examples of free, mixing, and trapped particles. A similar classification has been proposed for the perturbed vortex pair in uniform flow.[12,33]

Figure 8 displays a map of L^+ as a function of the fluid

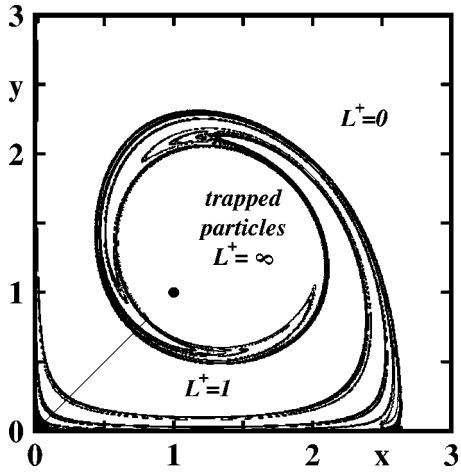

FIG. 8. Free, mixing, and trapped flow region for natural vortex motion with amplitude $R=0.5$. The curves display the boundary between the (integral) number of revolutions L^+ of a fluid particle around the vortex starting with initial position (x,y) and integrated at $t>0$. Trapped particles revolve infinitely long around the vortex ($L^+=\infty$). The solid circle represents the fixed point.

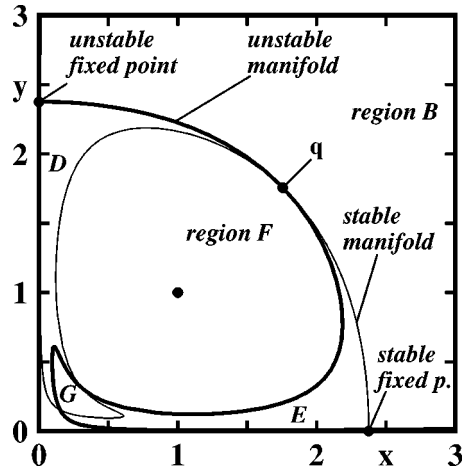

FIG. 9. Principal sketch of the Poincaré map including the fixed points on the axis, $\mathbf{x}_s$, $\mathbf{x}_u$, the invariant manifolds, W_s, W_u, and a primary intersection point $\mathbf{q}\in W_s\cap W_u$. The Poincaré map is constructed for natural vortex dynamics with amplitude $R=0.1$. The fixed point of the vortex dynamics is indicated by a solid circle at (1,1).

particle position (x_p,y_p) at $t=0$. The map of L^- is symmetric to L^+ with respect to the bi-sector $x=y$. The map of L can now easily be pictured as the sum $L^++L^-+L^0$. The free particles are located sufficiently far from the x and the y axis and outside a nearly circular region centered at the origin with a radius of about 2.65. The trapped particles are in a nearly circular region centered around the initial condition of the vortex, $x_v=y_v\approx 1.301$. The remaining particles are of the mixing type, i.e., spend a finite number of rotations around the vortex and then escape.

The map in Fig. 8 depends on the initial vortex position at $t=0$. Yet, the main characteristics of the map are preserved at other initial vortex positions on the periodic orbit.

C. Poincaré map

The dynamics of the fluid particles are described by a nonautonomous dynamics (9). For natural or controlled vortex motion with period T, the resulting velocity field has the same periodicity, i.e.,

$$\dot{\mathbf{x}}_p=\mathbf{F}(t,\mathbf{x}_p),$$

where $\mathbf{F}(t,\mathbf{x}_p)=\mathbf{F}(t+T,\mathbf{x}_p)$ for all $\mathbf{x}_p\in D$. This dynamics may be characterized by a Poincaré map from $\mathcal{D}$ into $\mathcal{D}$,[34]

$$\mathbf{x}^\star=\mathbf{\Phi}(\mathbf{x}), \tag{20}$$

where $\mathbf{x}$ represents the initial condition $\mathbf{x}_p=\mathbf{x}$ at time $t=0$, and $\mathbf{x}^\star$ is the fluid particle position $\mathbf{x}_p$ at time $t=T$.

At small amplitudes, the Poincaré map has (at least) three fixed points, one at the origin, one $\mathbf{x}_s$ on the x axes, and one $\mathbf{x}_u$ on the y axis (see Fig. 9). These hyperbolic points of the Poincaré map persist under perturbation. For notational brevity, we occasionally refer to $\mathbf{x}_s$ ($\mathbf{x}_u$) as the stable (unstable) fixed point according to the corresponding stability property of the wall-normal direction. However, both fixed points have stable and unstable directions aligned with the x axis and y axis, respectively.

The fixed point $\mathbf{x}_s$ ($\mathbf{x}_u$) has a stable (unstable) manifold $W_s(\mathbf{x}_s)$ ($W_u(\mathbf{x}_u)$) extending into the domain. Fluid particles which are on the stable (unstable) manifold at time $t=0$ will stay on this manifold at all positive (negative) integral multiples of the period $t=nT$, $n=1,2,\ldots$ ($n=-1,-2,-3,\ldots$). The manifolds intersect each other infinitely many times near the fixed points.[34] The fixed points and invariant manifolds can be shown to be symmetric with respect to the bi-sector $x=y$, since the vortex motion has the same symmetry and since the initial position of the vortex is on the $x=y$ line.

In particular, the invariant manifolds share a primary intersection point $\mathbf{q}$ on the bi-sector $x=y$ (see Fig. 9). Following [Ref. 12, Fig. 10(a)], this point is used to define the recirculation region $\mathcal{A}$. Let $\overline{\mathbf{x}_u\mathbf{q}}$ ($\overline{\mathbf{x}_s\mathbf{q}}$) denote the arc on W_u (W_s) from $\mathbf{x}_u$ ($\mathbf{x}_s$) to $\mathbf{q}$. The recirculation region $\mathcal{A}$ is defined as the interior of the closed curve consisting of the arcs $\overline{\mathbf{x}_u\mathbf{q}}$, $\overline{\mathbf{x}_s\mathbf{q}}$ and the sections on the axis from $\mathbf{0}$ to $\mathbf{x}_u$ and from $\mathbf{0}$ to $\mathbf{x}_s$. The free-stream region is denoted as $\mathcal{B}$.

The lobes of both manifolds must divide the first quadrant $\mathcal{Q}_I$ in infinitely many areas. A topological analysis can reveal how fluid particles move from lobe to lobe[12] using that a particle on an intersection point of $W_s(\mathbf{x}_s)\cap W_u(\mathbf{x}_u)$ must remain on this set and can only be mapped on another intersection point. Two of these lobes can easily be identified in Fig. 9: an entrainment lobe $\mathcal{E}$ near the x axis and the detrainment lobe $\mathcal{D}$ at the y axis (compare with Fig. 5 of Ref. 12). Fluid particles starting at $t=0$ in $\mathcal{D}$ are in the free-stream region $\mathcal{B}$ one period later, while fluid particles located in $\mathcal{E}$ came from $\mathcal{B}$ one period earlier. Figure 10 displays pathlines of selected fluid particles: two mixing particles starting at $t=0$ in the lobes $\mathcal{D}$, $\mathcal{E}$ and one trapped particle starting in region **F**.

A rigorous analysis of the lobe dynamics, like in Ref. 12, exceeds the scope of the present study. The following comments may illustrate the implications of Ref. 12 to Shu's recirculation zone model. Note that the other primary intersection points $W_s\cap W_u$ are very close to the fixed points.

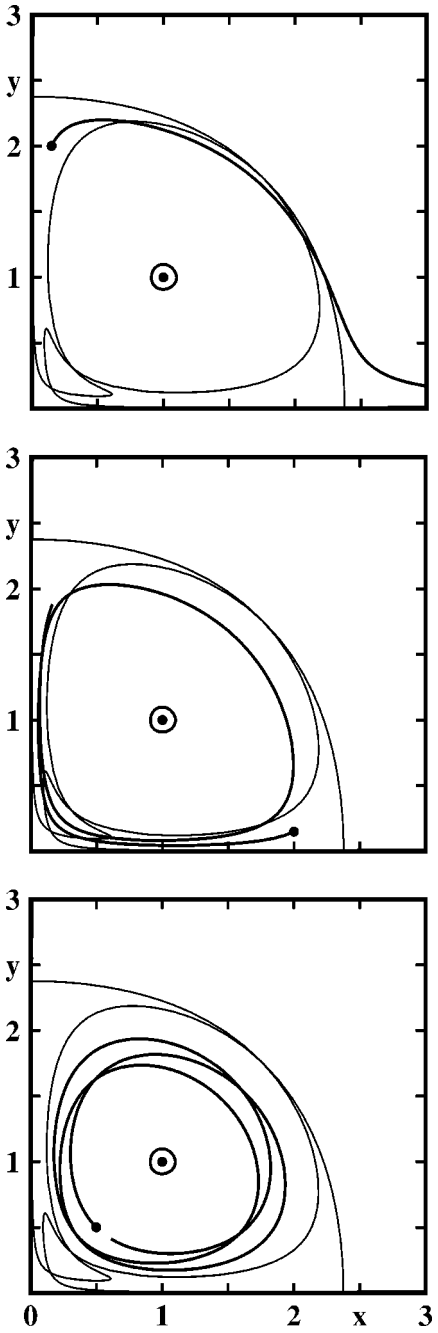

FIG. 10. Pathlines of fluid particles during one vortex period illustrating the implications of the Poincaré map in Fig. 9. The starting point of the fluid particles is marked by a solid circle and is situated in the detrainment lobe $\mathcal{D}$ (top), the entrainment lobe $\mathcal{E}$ (middle), and in the interior region $\mathcal{F}$ (bottom). The equilibrium point (1,1) of the vortex motion and its periodic orbit with radius $R=0.1$ is included.

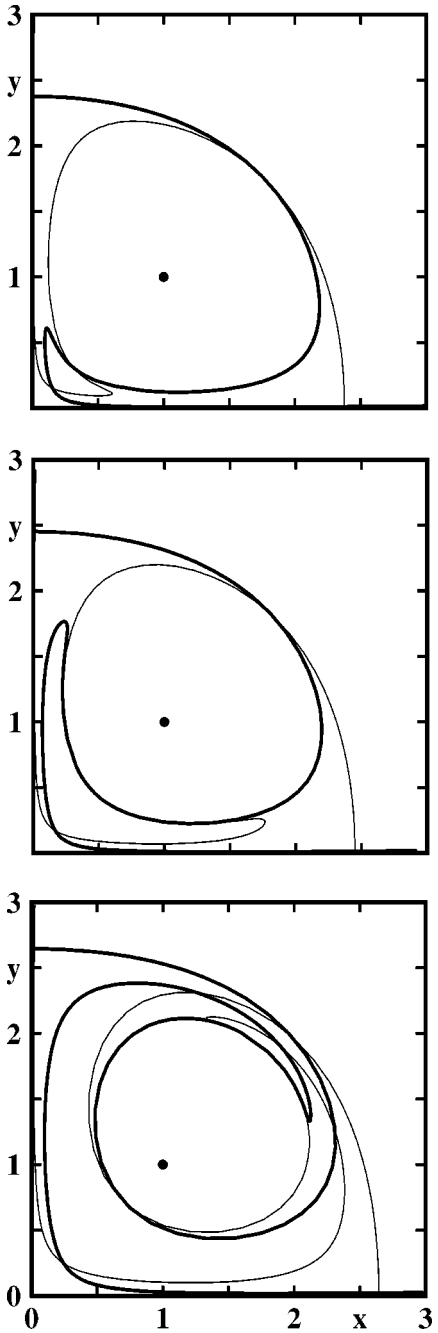

FIG. 11. Invariant manifolds of the Poincaré map for natural vortex motion at amplitudes $R=0.1$ (top), $R=0.2$ (middle), and $R=0.5$ (bottom). The solid circle represents the fixed point.

Thus far less lobes can be resolved in Shu's vortex model as opposed to the vortex pair representation of (Ref. 12, see Figs. 3 and 5). Neglecting other lobes, the area of the entrainment and detrainment lobes represent the flux through $\mathcal{A}$ integrated over one period—at least in the small amplitude limit. In this limit, the flux can quite generally be shown to be the sum of the lobe areas divided by one period using Melnikov's method.[12] For later reference, we call attention to the intersection region between the primary lobes $\mathcal{G}:=\mathcal{E}\cap\mathcal{D}$.

The lobe structure of the Poincaré map becomes more involved with increasing amplitude of vortex motion. Figure 11 displays the invariant manifolds at three different amplitudes. The Poincaré map considered in Fig. 9 is included for reasons of comparison.

The Poincaré map (Fig. 11, bottom) and the amount of particle revolutions around the vortex (Fig. 8) are associated with the same natural vortex motion. Apparently, the number of revolutions L^+ qualitatively resembles the lobe structure of the stable manifold $W_s(\mathbf{x}_s)$. A corresponding similarity can be observed for the residence times of the particles. As a good approximation, the stable and unstable manifold em-

brace the trapped region and the lobes belong to the mixing region.

D. Mixing measure

The invariant manifolds of the Poincaré map can be used to define a mixing measure. The curve $\mathcal{C}$ shall consist of the sections of the invariant manifolds from the fixed points to the first intersection point, i.e., $\overline{\mathbf{x}_s\mathbf{q}}$ and $\overline{\mathbf{x}_u\mathbf{q}}$ (see Fig. 9). At the considered parameters, the curve is nearly circular and represents the border between the recirculation region $\mathcal{A}$ and the free-stream region $\mathcal{B}$. In the limit of small amplitudes R, the curve $\mathcal{C}$ converges to the steady-state separatrix. With increasing R, the recirculation region grows as can be inferred from Fig. 11.

Mixing is associated with the behavior of an ensemble of fluid particles over a finite period of time. In a Hamiltonian system such as (9) it is known that good mixing occurs for unsteady perturbations of steady flows in the region near the separatrix.[8] In particular, it can be rigorously proven that some particles exhibit chaotic behavior. Kolmogorov–Sinai entropy was recently introduced as a measure of mixing in zones where flow is chaotic.[19] This entropy is for two-dimensional incompressible systems the integral of positive Lyapunov exponent over area. This quantity is, in the case of small unsteady perturbations to a steady flow, monotonically related to the flux over one period (which is the size of the lobe)[20] and in turn to Melnikov integral.[8] Thus, mixing may be expected to be increased if the fluid exchange across $\mathcal{C}$ is increased. In Sec. VI, the characterization of mixing is revisited from a more global perspective.

The instantaneous rate of fluid exchange is quantified by

$$Q=\int_{\mathcal{C}} ds\ |u_n|, \tag{21}$$

where ds represents an arc element of $\mathcal{C}$ and u_n the normal component of the velocity. A suitable mixing measure $\langle Q\rangle$ may be defined by the flux averaged over one period,

$$\langle Q\rangle=\frac{1}{T}\int_0^T dt\int_{\mathcal{C}} ds|u_n|. \tag{22}$$

The flux Q vanishes under steady-state conditions.

V. OPTIMAL MIXING

In Sec. IV, mixing of natural vortex motion is studied and a flux measure is suggested. In this section, an optimal mixing problem for controlled vortex motion is posed. First (Sec. V A), the mixing problem is defined. In Sec. V B, the employed numerical methods are described. In Sec. V C, the mixing enhancements due to control are outlined.

A. Optimal mixing problem

In this section, an optimal mixing problem is posed. This problem may be motivated by starting with a reconsideration of the natural vortex motion. The flux (22) in the recirculation zone can be increased without actuation by increasing the amplitude of vortex motion. Roughly, the flux is proportional to the amplitude. Engineering interest, e.g., in the case of recirculation zones in a combustor, is to maximize flux with a upper bound on the level of unsteadiness in flows to reduce material fatigue and undesirable instabilities. Increasing the flux further at given vortex amplitude requires actuation. Typically, limits on actuation shall assure efficiency.

The bound on the vortex motion shall be expressed in terms of the amplitude (10). The amplitude of actuation may be characterized by a corresponding quantity for a,

$$A:=\max_{\forall t}|a|. \tag{23}$$

In addition to the bounds on amplitude and on actuation, the controlled vortex motion is assumed to be periodic. This restriction significantly simplifies the solvability of the problem.

The set $\mathcal{V}(\Omega,R_{\max},A_{\max})$ of permissible controlled vortex motions $\mathbf{x}_v(t)$ is defined by the following four conditions.

(C1) The vortex motion is periodic with prescribed period T or, equivalently, with angular frequency $\Omega=2\pi/T$.

(C2) The vortex motion is bounded to a circular region with radius $R_{\max}$ centered at the equilibrium point, i.e., $R\leqslant R_{\max}$.

(C3) The actuation is bounded by $A\leqslant A_{\max}$.

(C4) The vortex motion and actuation satisfy the evolution equation (7) with control law (13).

The mixing optimization problem consists of finding a controlled vortex motion $\mathbf{x}_v^{\mathrm{opt}}$ in $\mathcal{V}(\Omega,R_{\max},A_{\max})$ which maximizes the flux $\langle Q\rangle$ (22). It should be noted that the recirculation region depends on the vortex motion.

The optimization problem may be reformulated in terms of the flat coordinate, i.e., by exploiting the controllability. Let $z_1(t)$ be the prescribed flat output function, then the second coordinate is given by $z_2=\dot{z}_1$. The associated vortex motion is defined by the inverse transformation (16). The associated actuation a is given by (13) realizing that $z_1=z_1^d$.

Let $\mathcal{Z}(\Omega,R_{\max},A_{\max})$ be the set of all differentiable functions $z_1(t)$ satisfying the following four conditions.

(D1) The flat coordinate has the period $T=2\pi/\Omega$.

(D2) The associated vortex motion $\mathbf{x}_v$ satisfies (C2).

(D3) The associated actuation a satisfies (C3).

(D4) The vortex motion and actuation satisfy (C4).

The optimization problem consists of finding the optimal flat output trajectory $z_1^{\mathrm{opt}}\in\mathcal{Z}(\Omega,R_{\max},A_{\max})$ which maximizes the flux $\langle Q\rangle$.

The equivalence of both optimization problems is easily seen. Condition (D4) is already fulfilled by construction. Hence, $\mathcal{V}(\Omega,R_{\max},A_{\max})$ and $\mathcal{Z}(\Omega,R_{\max},A_{\max})$ are equivalent. In addition, side constraints (C1)–(C3) and (D1)–(D3) are equivalent by construction.

Let us consider few limiting cases of the optimal mixing problem. Natural vortex motion is enforced by $A_{\max}=0$. The subset of natural motion $\mathcal{V}(\Omega,R_{\max},0)$ is always nonempty since the fixed point is contained in it. The optimal vortex motion is nontrivial if the frequency is realizable, $\Omega\leqslant 1$ (see

Fig. 3) and if the only vortex motion at prescribed period satisfies $R \leqslant R_{\max}$. On the other extreme, the optimal mixing problem with unbounded actuation $A_{\max}=\infty$ is likely to have no global solution as outlined in Appendix C.

B. Simplex algorithm

The search for a local maxima is carried out by a direct variational method and exploiting the reformulation in terms of the flat coordinate. This coordinate z_1 is approximated by a truncated Fourier expansion

$$z_1 = a_0 + \sum_{n=1}^{N} [a_n \cos(n\Omega t) + b_n \sin(n\Omega t)]. \tag{24}$$

The associated flux is denoted by $\langle Q \rangle^{[N]}$. In the following, $N=3$ is assumed. Thus, the flux is a function of seven Fourier coefficients, $\langle Q \rangle = \langle Q \rangle^{[3]}(a_0, a_1, a_2, a_3, b_1, b_2, b_3)$ subject to the side constraints (D2) and (D3). For reasons of simplicity, only symmetric controlled vortex motion with $b_1 = b_2 = b_3 = 0$ is considered.

Optimal local solutions are numerically found using a variant of the simplex method.[35] The side constraints are incorporated with by a penalty function, i.e., the following functional is maximized:

$$G := \langle Q \rangle - 10 \;\; H(A - A_{\max}) - 10 \;\; H(R - R_{\max}), \tag{25}$$

where $H(x)$ is the Heaviside function with $H=1$ at $x \geqslant 0$ and $H=0$ otherwise.

The amoeba in Ref. 35 has $N+2$ legs for $N+1$ coefficients $a_0, a_1, \ldots, a_N$. Initially, all legs are in the permissible set of Fourier coefficients corresponding to $A < A_{\max}$ and $R < R_{\max}$. This domain is numerically found to be locally convex. The amoeba crawls in the direction of maximum flux. When the amoeba wants to put one leg over a Heaviside cliff in Eq. (25), it immediately puts the leg back on safe permissible ground following the numerical recipes in Ref. 35.

The algorithm is stable and slow. It should be noted that each function evaluation requires the computationally involved determination of the unstable Poincaré manifold to determine the separatrix $\mathcal{C}$ for the flux. Different initial conditions for the amoeba have been tested. All simplex iterations converged to the same Fourier coefficients in the permissible range. This behavior indicates that the numerically found local maxima of G is either global or has a large range of attraction.

TABLE I. Optimal vortex motion defined by the flat coordinate $z_1^{\text{opt}}(t) = \Sigma_{n=0}^{3} a_n \cos n\Omega t$. The solution of the optimal mixing problem assumes the bounds on the vortex and control amplitude, i.e., $R = R_{\max}$ and $A = A_{\max}$, respectively.

Ω	0.8	1.0	1.2
a_0	1.1294	1.1049	1.1353
a_1	0.5894	0.5827	0.4152
a_2	−0.0566	−0.0608	0.0176
a_3	0.0655	0.0435	0.0129
R	0.5	0.5	0.5
A	0.5	0.5	0.5
$\langle Q \rangle$	2.3417	2.0736	1.1469

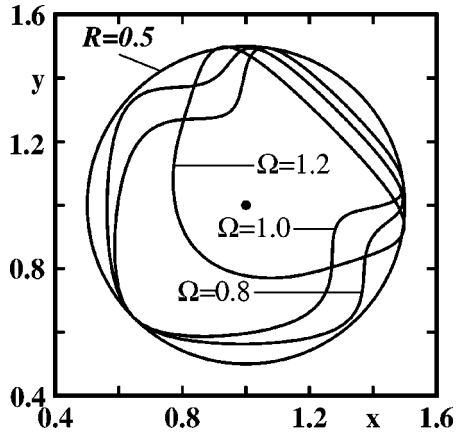

FIG. 12. Optimal controlled vortex motions at $\Omega = 0.8$, 1, and 1.2 subject to $R \leqslant 0.5$ and $A \leqslant 0.5$.

C. Mixing enhancements

In this section, the numerical solutions for the optimal mixing problem at $R_{\max}=A_{\max}=0.5$ and for selected frequencies Ω are discussed.

Table I enumerates the achieved fluxes $\langle Q \rangle$ with an optimal flat coordinate z_1^{opt} based on expansion (24) with $N=3$. The vortex motion is illustrated in Fig. 12 for the optimal numerical solutions of Table I. Apparently, the optimal orbits touch the circular permissible region. From Table I, also the maximum bound on control can be seen to be assumed by the optimal orbits. The high-frequency buckles in the orbits increase the actuation and thus contribute to the flux. At $\Omega = 1.2$, i.e., above the range of natural frequencies, the permitted actuation amplitudes $A_{\max}=0.5$ is not large enough to yield a more full vortex orbit and the achievable flux falls sharply. In Appendix C, the effect of the side-constraints in limit $\Omega \to \infty$ is discussed.

The frequency dependency of optimal flux under the given side-constraints is shown in Fig. 13. For the natural frequency range, $\Omega < 1$, actuation increases the flux noticeably as compared to natural vortex motion with the same amplitude $R=0.5$.

Evidently, a larger flux can be achieved by lowering the frequency. However, the frequency may also be employed to control another aspect of mixing, for instance, the residence time distributions of the fluid particles in the recirculation

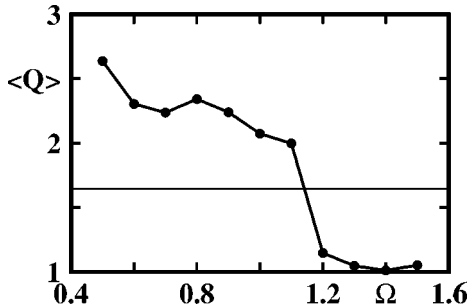

FIG. 13. Averaged flux $\langle Q \rangle$ associated with optimal controlled vortex motions at $\Omega = 0.5$ to 1.5 subject to $R \leqslant 0.5$ and $A \leqslant 0.5$. The horizontal line refers to the flux associated with natural vortex motion at $R=0.5$.

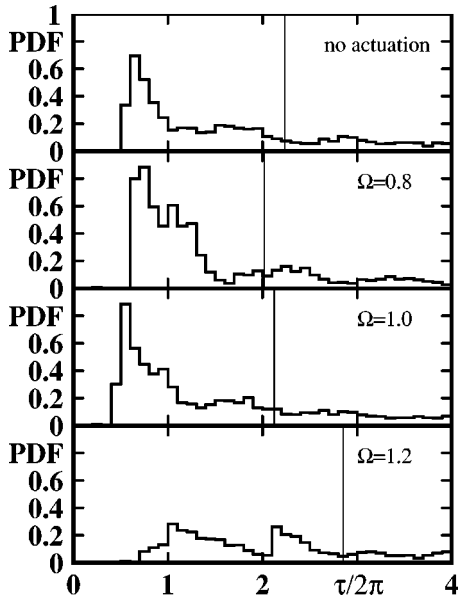

FIG. 14. Residence time distribution τ of mixing particles under natural (top) and optimal vortex motion (below) at $\Omega=0.8$, $\Omega=1$, and $\Omega=1.2$. The thin vertical line indicates the average residence time. The recirculation region is defined by the Poincaré map for the associated vortex motion. The considered fluid particles start in the recirculation region at $t=0$. The PDFs are normalized to yield the area of the mixing particles upon time integration.

zone $\mathcal{A}$. The residence time τ is defined as the total time which a mixing particle spends during its history $-\infty<t<\infty$ in the recirculation region. Only mixing particles are considered which are in $\mathcal{A}$ at $t=0$. Thus, the escape of particles can be monitored. Figure 14 shows the probability density functions (PDF) based on an ensemble of 500×500 particles in the region $0<x,y<3$. The PDFs are normalized so that the integral over the complete distribution is the ratio of the mixing region to the complete recirculation zone. The average residence time is indicated by the thin vertical line in Fig. 14. This time increases with increasing frequency.

Flux and residence time behavior can be explained with the Poincaré maps associated with the optimal vortex motion (Fig. 15). The area of the lobes indicate the mass ejected per period. This area at $\Omega=0.8$ is significantly larger than the one at $\Omega=1.2$. Hence, the flux at $\Omega=0.8$ can be expected to be larger, even correcting for the smaller period at $\Omega=1.2$. At $\Omega=0.8$ and 1.0, the overlap region $\mathcal{G}:=\mathcal{D}\cup\mathcal{E}$ represents a significant portion of $\mathcal{D}$ and $\mathcal{E}$. Particles in $\mathcal{G}$ have been absorbed from the free-flow region $\mathcal{B}$ less than a period ago and are ejected to $\mathcal{B}$ during the next period. Hence, the residence time τ of these particles in $\mathcal{A}$ is between $0<\tau<2\,T$, say, around one period. The large overlap region $\mathcal{G}$ thus explains the pronounced single maximum in the residence time PDF. At $\Omega=1.2$, the overlap region is small and a significant portion of the fluid in the entrainment lobe $\mathcal{E}$ (see Fig. 9) has to wait at minimum another period before it moves to the detrainment lobe $\mathcal{D}$ where it gets ejected in the following cycle. Hence, the PDF has two pronounced maxima associated with areas $\mathcal{D}\cap\mathcal{E}$ (first maxima) and with $\mathcal{E}-\mathcal{D}$ (second maxima). The PDF is also flatter partially due to the larger residual region $\mathcal{A}-\mathcal{D}-\mathcal{E}-\mathcal{F}$.

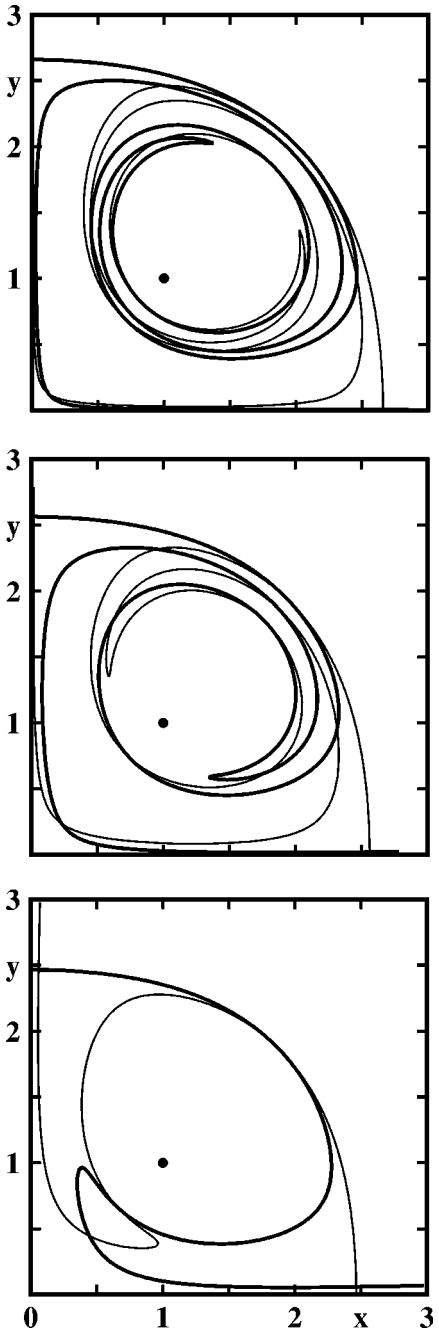

FIG. 15. Same as Fig. 11, but for optimal vortex motion at $\Omega=0.8$ (top), $\Omega=1$ (middle), and $\Omega=1.2$ (bottom).

Rom-Kedar, Leonard, and Wiggins[12] observe significantly longer residence times over dozens of periods for their periodically perturbed vortex pair. The difference can be explained by the large amount of dynamically relevant lobes in their Poincaré map. In contrast, the displayed Poincaré maps for Shu's model appear to be dominated by two lobes and their overlap region. In a later study, Rom-Kedar and Poje[33] prove that the flux vanishes in the limits $\Omega\to0$ and $\Omega\to\infty$ for a large class of Hamiltonian dynamics, including the vortex pair model. These aspects are considered in Appendixes B and C.

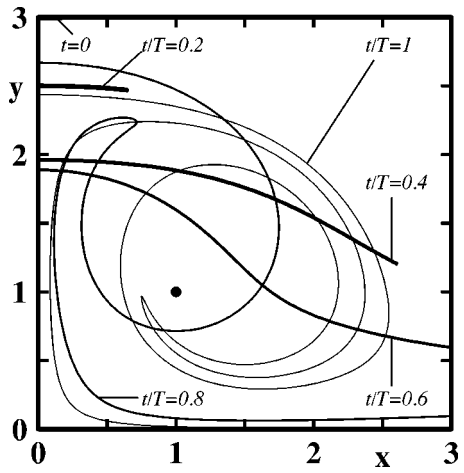

FIG. 16. Stretching and folding of a material fluid particle line at $t/T=0$, 0.2, 0.4, 0.6, 0.8, and 1. The vortex motion is the solution of the optimization problem at $R_{\max}=0.5$ and $\Omega=1$. The thickness of the material curves decreases with increasing time. The equilibrium point of the vortex at (1,1) is indicated as a solid circle.

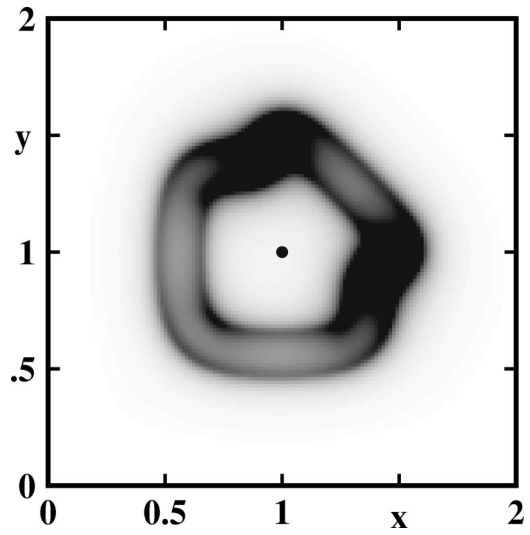

FIG. 17. Averaged Okubo–Weiss parameter for the vortex motion of Fig. 16. The value of this parameter is indicated as an interpolated gray tone from white at 0 to black at -2000 or less. The equilibrium point of the vortex at (1,1) is indicated as a solid circle.

VI. MIXING CHARACTERIZATION

In this section, the flux-based mixing optimization in Sec. V is related to other mixing characterizations and goals. While the employed mixing measure is elegantly related to the Poincaré map analysis, it may not be aligned—even contradict—other mixing goals. In Sec. VI A, the qualitative implications of mixing, i.e., stretching and folding, are illustrated for the recirculation zone. In Secs. VI B and VI C, Eulerian and Lagrangian measures of stretching are discussed. In Secs. VI D and VI E, good mixing between two fluids and two regions is quantified for the recirculation zone. Finally (Sec. VI F), a refined mixing measure is proposed for combustor-related problems. All results presented in this section refer to the optimal vortex motion of Sec. V C at frequency $\Omega=1$ and oscillation amplitude $R=0.5$ if not stated otherwise.

A. Qualitative consideration of stretching and folding

The qualitative implication of mixing is a process with stretching and folding of fluid particles.[6,7] Figure 16 illustrates this process for a material line of fluid particles. The material line is released on a section $0\leqslant x\leqslant 0.2$ of the horizontal line $y=3$ at $t=0$. Evidently, this curve experiences a significant amount of stretching before fluid particles get folded in the mixing region. In contrast, material lines outside the mixing region are only stretched by the dominant stagnation point flow and are not folded.

Typically, the stretching and folding process of laminar flow in a closed domain is associated with a nonvanishing shear rate of the velocity field, with an exponential divergence of infinitesimally close fluid particles, and with a more uniform distribution of initially distinct groups of fluid particles. While all these properties are typically desirable, the attempt to quantify good mixing is a difficult and subjective undertaking.[6,7]

B. Eulerian stretching measures

A necessary but not sufficient condition for a good fluid mixer is a nonvanishing strain rate of the velocity field. An example of a good mixer is Aref's blinking vortex model.[5] An example of a bad mixer is a single Oseen vortex in ambient flow, since the fluid particles cannot escape the circular streamlines.

The Okubo–Weiss parameter is often used to discriminate between good and bad strain rates. For planar flow, this parameter is defined as the determinant of the velocity Jacobian, $\lambda:=\det(\nabla\mathbf{u})$. The parameter is positive for regions with solid-body-like rotation and small fluid exchange and is negative for saddle-point-like regions which enhance stretching. Figure 17 illustrates the time-averaged Okubo–Weiss parameter for the recirculation-zone model. Evidently, the valley of this parameter follows closely the orbit in Fig. 12. This behavior is not surprising, since the instantaneous parameter has a sharp singularity at a potential vortex which scales with r^{-4}, where r represents the distance to the vortex. For the numerical computation, the vortex has been regularized by a Rankine core of radius 0.05.

Hence, the Okubo–Weiss parameter does not appear very useful for characterizing mixing in the recirculation zone. This parameter may be more appropriate for less singular vorticity distributions, for instance a von Kármán vortex street.

C. Lagrangian stretching measures

Eulerian stretching measures like the Okubo–Weiss parameter can be conveniently computed. However, the long-term effect of stretching on individual fluid particles is more adequately quantified by a Lagrangian quantity. This quantity follows the fluid particles and monitors their neighborhoods over a period of time. The most prominent example is the largest Lyapunov exponent.

The infinite-time Lyapunov exponent characterizes well

the stretching in a finite domain of which the fluid particles cannot escape. For the mixing particles of the recirculation zone, these exponents adopt the value k of (1), i.e., characterizes the stretching of the far-field stagnation point flow $dx/dt=kx$, $dy/dt=-kx$. For a finite mixing region in uniform flow, the exponent even vanishes for almost all fluid particles.[12] The applicability of finite-time Lyapunov exponents has been studied extensively by Rom-Kedar, Leonard, and Wiggins.[12] Those authors suggest the stretching ratio of fluid particles before and after the mixing zone as an alternative mixing measure to the Lyapunov exponent. This ratio is, of course, preserved in uniform free stream motion. In Shu's model, however, such a definition is complicated by the saddle point flow in the far field, i.e., a continued stretching outside the mixing region. Thus, any finite-time stretching analysis for Shu's model has a large subjective bias. We shall not pause to carry out such a study.

D. Two fluid mixing

The discussions of the preceding sections directly relate to the stretching and folding of fluid particles. A variety of flow control applications target more specifically at a good mixing between two kinds of fluids. For instance, boundary-layer separation in an adverse pressure field may be delayed by a good mixing between high-momentum fluid of the free stream with the low-momentum fluid in the near-wall region.[1] In a combustor, as another example, good mixing shall be achieved between the incoming cold and fuel rich fluid and the hot combustion products in the recirculation region.

A necessary but not sufficient condition of efficient two-fluid mixing is a nearly constant concentration c of each specimen. A uniform distribution maximizes the information entropy

$$I := -\int dV\, c \ln c, \tag{26}$$

which can thus be taken as a quality measure.[19,36]

Targeting combustion-related problems, the entropy (26) with the mixing particle concentration may be taken as an alternative measure. Let $\tau(x_0,y_0,t_0)$ be the residence time of a fluid particle passing through $\mathbf{x}=\mathbf{x}_0$ at time $t=t_0$. This residence time accumulates all periods of times in $\mathcal{A}$ during the whole life of the particle $-\infty<t<+\infty$. The characteristic function for the mixing particles is given by $\chi(x_0,y_0,t_0)=1$ if $\tau(x_0,y_0,t_0)>0$ and zero otherwise. The concentration c is defined by the time average of the characteristic function,

$$c(x,y) := \langle \chi_c(x,y,t) \rangle. \tag{27}$$

Figure 18 visualizes the concentration distribution. The concentration vanishes around the equilibrium point of the vortex and in the free stream. The distribution has a hill around the core and near the axes. The figure indicates a smooth decline of the concentration near the inflow $y=3$. Particles released in the interval $0.5<x<1$ may or may not be entrained in $\mathcal{A}$ depending on the instant of the release.

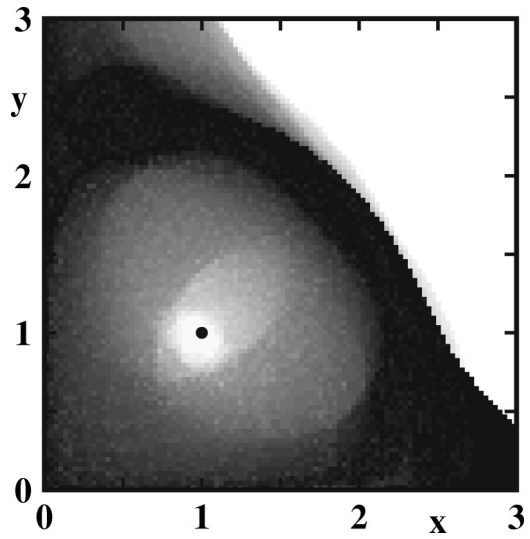

FIG. 18. Concentration $c_C(x,y)$ of mixing particles for the vortex motion of Fig. 16. The value of the concentration is indicated by an interpolated gray tone from white at 0 and black at 1. The equilibrium point of the vortex at (1,1) is indicated as a solid circle.

The entropy I based on this concentration decreases from 1.37 for natural vortex motion at $R=0.5$ to 1.13 for optimal vortex motion at $R=0.5$ and $\Omega=1$. In other words, the optimization of the flux by actuation leads to a decrease of the uniformity measure, indicating an inverse correlation between both quantities. Indeed, the integral (26) is correlated with the area where the concentration is near the maximum of $c \ln c$ on $0 \leqslant c \leqslant 1$, i.e., near $c \approx 1/e$. For open flow problems, the flux due to mixing particles need not be related to the entropy. An enhanced entropy may, for instance, be caused by more unsteady lumps of mixing particles which do not entrain other fluid. For confined flow, however, an instantaneous entropy measure has successfully been employed to monitor mixing enhancement.[36] Like the Lyapunov exponent, the entropy may be more adequate for the characterization of confined flow.

E. Two region mixing

The underlying assumption of the two-fluid consideration is that their properties become homogenized by stretching and folding, while the fluid particle advects its unchanged property. A related view is a flux between two regions $\mathcal{A}$ and $\mathcal{B}$. Here, the underlying assumption is a desirable transformation of a fluid-particle property as it passes from one region to another one. An example is, again, the combustor, where the fuel-rich cold fluid from the oncoming flow $\mathcal{B}$ shall ignite as it passes in the hot recirculation region $\mathcal{A}$. In this framework, the flux appears a good candidate for a mixing measure.

From a chemical perspective, the residence time of a fluid particle in the dead-water region $\mathcal{A}$ is an important parameter. If the residence time is larger than the ignition time, the particle has undergone the desired transformation from a cold to a hot particle. Figure 19 displays the residence-time distribution $\tau(x,y,t)$ of all fluid particles which are in $\mathcal{A}$ at time $t=0$. The nearly circular core around

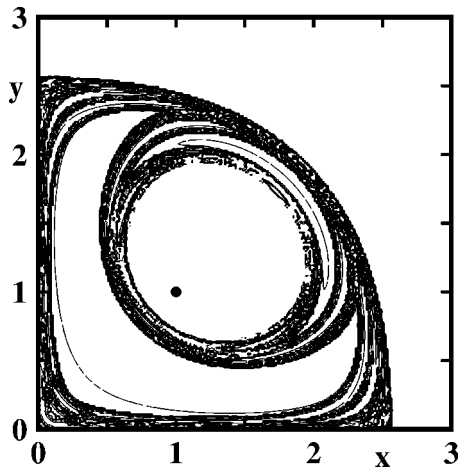

FIG. 19. Spatial residence time distribution $\tau(x,y)$ for the vortex motion of Fig. 16. The contour curves represent $\tau/T=0.5,1,1.5,2,\ldots,10$. The equilibrium point of the vortex at (1,1) is indicated as a solid circle.

the vortex equilibrium point has an infinite residence time. In contrast, the large white banana-shaped region represents a region with small residence time $\tau<T/2$. The resulting PDF of the residence time of all mixing particles has been displayed in Fig. 14 and been discussed in Sec. V C. It should be noted that $\tau(x,y,0)$ is symmetric with respect to the bisector $x=y$, since the residence time comprises the past and the future of the particle in $\mathcal{A}$. In contrast, the loop number distribution L^+ in Fig. 8 is asymmetric since only the future $t>0$ has been considered.

Figure 20 (top) illustrates the depletion of fluid particles which were initially in the recirculation zone $\mathcal{A}$. The depletion function $F(t)$ is defined as the ratio between the area of fluid particles which are in $\mathcal{A}$ at time t and the corresponding area at the initial instant. F converges to a finite value which is the ratio between the core defined by $\tau(x,y,0)=\infty$ and the

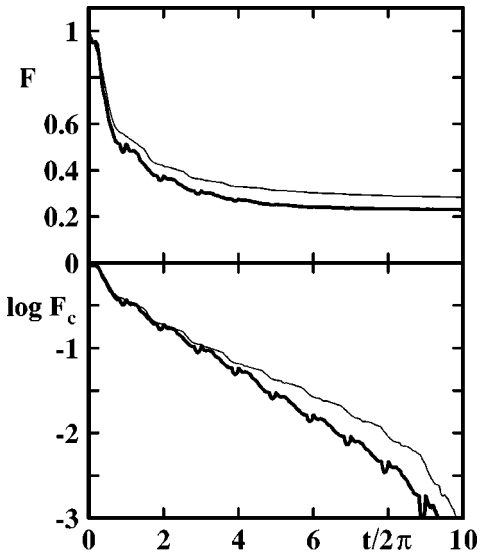

FIG. 20. Depletion of particles from the recirculation zone for the vortex motion of Fig. 16 (thick line) and the natural vortex motion with the same amplitude (thin line). The top figure displays F, and the bottom one $\log_{10} F_C$.

recirculation region. Evidently, the enhanced flux by control action has decreased the amount of trapped particles as compared to natural vortex motion which is indicated by the thin line.

Figure 20 (bottom) illustrates the depletion function $F_c(t):=(F(0)-F(t))/(F(0)-F(\infty))$ containing only the mixing particles. In a good approximation, the decay is exponential with a half-time of 0.93 T. For natural vortex motion, the decay is smaller and does not follow an exponential law. An analogous mixing analysis of the perturbed vortex pair also yields parameters with and without exponential decay (see their Figs. 16 and 17 in Ref. 12).

F. A refined mixing measure

The mean flux $\langle Q\rangle$ through the recirculation zone is induced by mixing or by trapped particles. Free particles have, by definition, a vanishing residence time in $\mathcal{A}$ and can thus not contribute to the flux. Mixing particles entering $\mathcal{A}$ will eventually leave $\mathcal{A}$ and thus contribute two times to the flux. Hence, $\langle Q\rangle/2$ is the upper bound for the flux of new particles entering $\mathcal{A}$.

This conditioned flux $\langle Q\rangle_c$ can be expressed in terms of the characteristic function,

$$\langle Q\rangle_c := -\left\langle \int_0^\infty dx\, v(x,y_{\text{inflow}},t)\chi_c(x,y_{\text{inflow}},t)\right\rangle. \qquad (28)$$

The inflow boundary has been set to $y_{\text{inflow}}=3$ which guarantees $v<0$ at all times and is well above the recirculation region. However, the definition is independent of y_{inflow} as long as no backflow $v<0$ can occur. In addition, the x integration in (28) can be restricted to $0\leqslant x<3$, since $u>3$ at all $x\geqslant 3$, $y\geqslant 0$. In other words, no fluid particles released at $x>3$ and $y=3$ will enter the recirculation region, i.e., the characteristic function $\chi_c(x,3,t)$ vanishes identically.

The conditioned flux is numerically computed by continually releasing fluid particles at the inflow boundary $y=3$, $0<x<3$. The particle passing the x interval $[x,x+dx)$ in the time interval $[t,t+dt)$ has the area $-v(x,3,t)\,dt\,dx$. The resulting conditioned flux is 90% of the upper bound $\langle Q\rangle/2$. This implies that only 10% of the flux are induced by mixing particles passing through the recirculation region more than once or by trapped particles.

The conditioned flux elucidates that the chosen ensemble of considered fluid particles can effect the mixing measure. Figure 21 displays the ensembles considered so far.

(i) An ensemble of mixing particles which are released at the inflow boundary $y=3$ at $0\leqslant t<T$, called *flux ensemble* in the following.
(ii) A Poincaré ensemble of mixing particles released in the x,y plane at $t=0$.
(iii) A statistical ensemble of mixing particles released at $0\leqslant t<T$ in the x,y plane.

The Poincaré ensemble dominates the current study since mixing can be described and understood in terms of the lobe dynamics. The statistical ensemble has been employed for the concentration study of Sec. VI D.

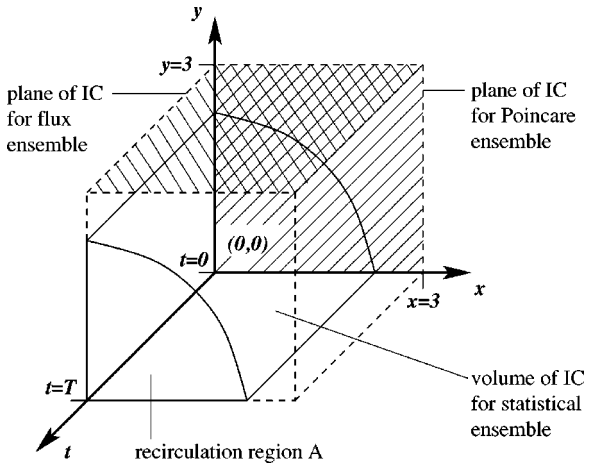

FIG. 21. Principal sketch of the considered fluid particle ensembles. A mixing particle of a given ensemble has a trajectory with an initial condition (IC) on the specified plane or in the specified rectangle and which passes the recirculation region $\mathcal{A}$ at least once.

The effect of the choice of the ensemble can be significant. This is shown in Fig. 22 for the distribution function $P(t)$ of the Poincaré and flux ensemble. This function $P(t)$ is the normalized integral over the PDF and specifies the percentage of particles with residence times $\tau<t$. The average residence time of the mixing particles of the Poincaré ensemble is 2.25 T whereupon the corresponding value of the flux ensemble is 0.66 T. The flux ensemble comprises also many mixing particles released at the inflow section $y=3$, $0.5<x<1$ around $t\approx 0.5$ which briefly scratch the boundary of the recirculation zone and thus reduce the residence time. These particles are not contained in the present Poincaré ensemble focusing on the times $t=nT$, $n=\cdots, -1,0,+1,\ldots$. It may be noted that this discrepancy is largely an artifact caused by the definition of the mixing particles via $\tau>0$ in a more or less arbitrarily defined recirculation region. The discrepancy is much smaller if only fluid particles with a nonvanishing and finite number of loops L around the vortex are counted. The characteristic function in the conditioned flux may be easily be tuned to include only those particles of interest, e.g., particles with $0<L<\infty$ instead of $0<\tau<\infty$. In the small-amplitude limit, both considerations may coincide under suitable conditions.

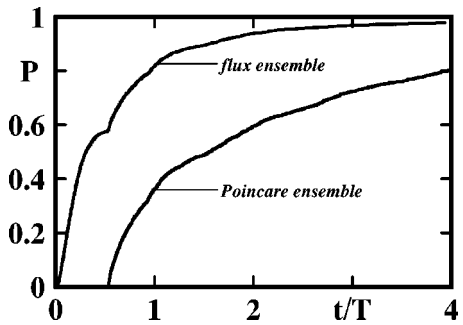

FIG. 22. Distribution function P of the residence times of the mixing particles. The distribution function of the Poincaré ensemble is compared with the pendant of the flux ensemble.

In addition to the choice of the ensemble, the definition of the recirculation zone has to be revisited if no Poincaré map is available, e.g., for nonperiodic flow. In this case, we suggest following definition of a recirculation region: the interior part of the boundary curve of this region shall (i) connect the x and y axis, (ii) enclose the vortex, and (iii) minimize the time-averaged flux with respect to infinitesimal curve deformations. The influence of the chosen ensemble and chosen definition of the recirculation region on the given mixing measure requires an extensive parametric investigation and might serve as an inspiration of some future studies. This definition of the recirculation zone, the flux ensemble, and the conditioned flux (28) can be applied to a large class of periodic and nonperiodic flows.

VII. TRACKING WITH OBSERVATION-BASED FEEDBACK

The feedback flow control of the preceding sections requires the knowledge of the vortex position at all times (complete information control). In this section, an observer is designed which determines the vortex position (x_v, y_v) from a single-component fluid velocity sensor near the wall. Thus, a single-input control based on wall measurements may be designed. A global observer for all velocity position is difficult to construct because of the level of nonlinearity in the vortex model. Hence, we trade globality for simplicity and for robustness and develop in Sec. VII A a constant structure/gain observer that will be valid in a neighborhood of the equilibrium point $(x_v, y_v)=(1,1)$. That neighborhood will be large enough to include optimized reference vortex trajectories. In Sec. VII B, a simple dissipative controller will be used to drive the vortex from the far field to the observer domain. This controller does not need an observer. In Sec. VII C, the switching algorithm between the near-field observer and far-field controller is outlined. More details are provided in Refs. 37 and 38.

A. Observer design

In this section, an observer is designed based on a linearization around the equilibrium point of the vortex motion (1,1). Let (u,v) denote the (normalized) Cartesian components of fluid velocity. In our viscosity-free idealization, a fluid velocity sensor will be located at a wall point $(\alpha,0)$, $\alpha>0$. The transversal component v vanishes because of the no-penetration condition. The tangential velocity component u is given by

$$u=\partial_y(1+a)\Psi_c+\Psi_v)|_{x=\alpha,\,y=0}$$
$$=\frac{1}{2}(1+a)\alpha-\frac{8\alpha x_v y_v}{(x_v^2+y_v^2+\alpha^2)^2-4\alpha^2 x_v^2}. \tag{29}$$

Since the component $(1+a)\ \alpha/2$ of u adds no information, we shall use a modified definition of the observation signal $U=u-(1+a)\ \alpha/2$, where this component is removed. Moreover, we focus on the selection of $\alpha=1$, by which the sensor is closest to the unactuated equilibrium point.

The observer is based on the same flat coordinates used for tracking control. The dynamic observer is based on the

integration of a duplicate of Eq. (17) adding a linear feedback term. This feedback term vanishes if the correct location in state space has been found and the term corrects the observer system in proportion of the difference between observed and predicted signal. The dynamic observer reads

$$\begin{aligned}\dot{\hat{z}}_1 &= \hat{z}_2 + \zeta_1(\hat{U}-U),\\ \dot{\hat{z}}_2 &= \hat{p} + a\hat{q} + \zeta_2(\hat{U}-U),\end{aligned} \tag{30}$$

where the hat "ˆ" indicates an estimated variable. In particular, $\hat{p}$, $\hat{q}$, and $\hat{U}$ are obtained by evaluating p, q, and U, at $\hat{z}_{1,2}$ and where the correction terms ζ_i are to be determined by the measured tracking error $\delta U = \hat{U} - U \approx \partial_{z_1} U \cdot \delta z_1 + \partial_{z_2} U \cdot \delta z_2$. The simplest option is that of using a constant linear gain $\zeta_k(\hat{U}-U) = -L_k \delta U \approx -L_k(\partial_{z_1} U \cdot \delta z_1 + \partial_{z_2} U \cdot \delta z_2)$. This linearization leads to a small-deviation model for estimation-error dynamics

$$\frac{d}{dt}\begin{bmatrix}\delta z_1\\ \delta z_2\end{bmatrix} = \begin{bmatrix}A_{e,11} & A_{e,12}\\ A_{e,21} & A_{e,22}\end{bmatrix}\begin{bmatrix}\delta z_1\\ \delta z_2\end{bmatrix}, \tag{31}$$

where

$$\begin{aligned}A_{e,11} &= -L_1 \partial_{z_1} U,\\ A_{e,12} &= 1 - L_1 \partial_{z_2} U,\\ A_{e,21} &= -\left(\frac{1}{z_1^2}(1-z_2^2) + L_2 \partial_{z_1} U\right),\\ A_{e,22} &= 2z_2\left(1 + a - \frac{1}{z_1}\right) - L_2 \partial_{z_2} U.\end{aligned}$$

The selection of gains L_i should stabilize this system. A heuristic guidance comes from Tadmor and Banaszuk[38] where Lyapunov stability analysis is carried out of the frozen time system, i.e., matrix A_e is evaluated at a constant point z. It is a basic fact that if $A_{e,11}$, $A_{e,22} \leqslant 0$ and not both zero, and if $A_{e,12} \cdot A_{e,21} < 0$ then the frozen time system is stable. The signs of $\partial_{z_1} U$ and $\partial_{z_2} U$ determine what values of L_i bring A_e to that form. A numerical computation (omitted here) reveals that both $\partial_{z_k} U$, $k = 1,2$, are positive over the neighborhood of interest of the equilibrium point (1,1). This suggests a selection of $L_1 = 0$ and of a sufficiently positive L_2.

Our use of a tentative language is due to the fact that stability of each frozen time system might not imply (or be implied by) stability of a time varying/nonlinear system. Local stability has thus to be verified by additional analysis or numerical simulations. Since we are interested in a near-periodic behavior, our analysis was based on a very low order (third harmonic) approximate dynamic phasor model[39] which was linearized about the reference trajectory. The dynamic phasor model describes the dynamics of harmonic coefficients in a Fourier expansion over a sliding interval $[t-T, t]$, of a near-T-periodic signal. It is derived from the original differential equation, governing the time trajectory. The approximate model is obtained by compression to a few low harmonics, with inevitable distortions in a highly nonlinear system, such as ours. The advantage of the phasor model is that each periodic trajectory is represented by a single point, and linearization about that point is time invariant. This enables stability analysis in terms of eigenvalue locations, as a function of design gains. Figure 23 depicts the maximal real parts of these eigenvalues, as a function of L_2, for a number of reference trajectories. As it turns out, its predictions are conservative. However, it does provide an indication of stability and guidance for the selection of $L_2 \in [1,2]$.

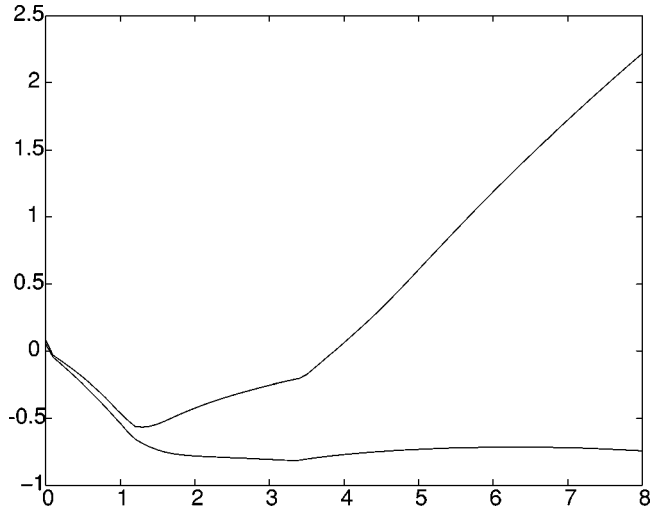

FIG. 23. The maximal real parts of eigenvalues of the localized phasor dynamics model as a function of the gain L_2 (with $L_1 = 0$) for two nominal trajectories.

B. A simple dissipative measurement feedback

In this section, we describe a feedback policy that uses sensor readings to drive the vortex from the far field into the observer domain. In the absence of an observer, it is based on the dynamics of stored energy,

$$\frac{d}{dt}((1+a)\ \Psi_c + \Psi_{\mathrm{mv}}) = \dot{a}\Psi_c. \tag{32}$$

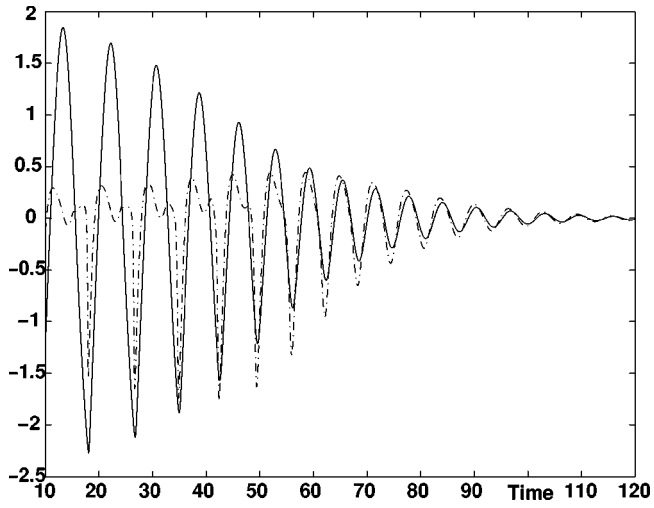

FIG. 24. Plots of z_1 (solid) and a (low pass filtered) $u - \overline{u}$ (dashed) under low gain actuation that stabilizes the equilibrium point.

By Eq. (32), any control satisfying $\dot{a}\Psi_c<0$ is dissipative, and drives the vortex towards the equilibrium point. Moreover, under low-gain actuation and a nearly periodic dynamics, the same holds if $\dot{a}(\Psi_c-\overline{\Psi}_c)<0$, where $\overline{\Psi}_c$ is the average over a period and $\dot{a}$ is zero mean. Figure 24 shows $\Psi_c-\overline{\Psi}_c$ and $U-\overline{U}$ as a function of time. Here, U is a low-pass filtered version of the observation signal. This filter is based on a normalized cut frequency of 0.5 rad, or half the nominal natural frequency of vortex motion, near the equilibrium point. These trajectories are associated with a trajectory of the original system that spirals towards the equilibrium point. The phase match is obvious. During large deviations we thus implement a low gain negative integral feedback $\dot{a}=-\delta(U-\overline{U})$. In fact, the trajectory used in Fig. 24 was obtained under this policy.

The following comments concern some practical issues of that policy. First, it is noted that in order to implement it, one needs to be able to estimate both the instantaneous period of the unactuated (or low-gain actuated) system and of the instantaneous level of its stored energy. The period is needed to compute $\overline{U}$. The level of stored energy is used as an indication of vortex residence in the domain of observer stability, and thus, as a trigger for the switch to an observer based tracking control. A surrogate for the fluctuation level in (nearly) periodic motion is the value of $z_1=\Psi_c$, at the trajectory's intersection with the ray $\{z:z_2=0\}=\{(x,y):x=y\in(0,1]\}$. Simulations (left out here) reveal monotonous dependencies of both, the period and the fluctuation level on the minimum absolute value of U, over a period. These dependencies can thus be tabulated and used in the suggested control scheme. Since period length ranges between $[2\pi, 10.5]$ time units, the minimum of $|U|$ over an 11 time units interval is identical to the needed minimum over a period, and is used for that purpose.

A second issue concerns the fact that the calculated $U-\overline{U}$ is not perfectly zero mean. Under pure integration, accumulated errors will create an undesirable drift in a. As a matter of standard practice, the pure integrator is replaced by a low-pass filter [say $1/(s+0.1)$].

In closing, it is worth noting that the energy shaping scheme can be utilized also in simple tracking tasks, where the target orbit is an equipotential orbit of the uncontrolled system. Examples are provided in Ref. 38.

C. The combined compensator

The combined compensator is based on patching of the two control modes suggested above. Switching between different controllers is a delicate job, even under more favorable circumstances, where a detailed observation is available. Issues include stability under the switching procedure and avoiding chatter. We used a relatively simple hysteretic heuristic for the switching logic, as follows. An indicator for leaving the observer region is triggered either by the observer state leaving a set neighborhood of (1,1), or when the minimum $|U|$ over a fixed period descends below a set threshold. Two thresholds are used. When the first (higher) level is crossed, the observer state is considered unsafe for control decision. The feedback controller then switches to the dissipative mode, but the dynamic observer continues. When the lower level is crossed it is concluded that the observer might run into instability, and its dynamics are replaced by a stable, oscillatory second-order dynamics with an equilibrium point at $\hat{z}=(1,0)$, a long time constant and a period compatible with higher fluctuation levels of the unactuated system. The purpose of the first modes is to safely return the vortex to the stability zone. The purpose of the second mode is to safely drive the observer state into the stability zone. Additionally, a key aspect of the switch mechanism is a hysteretic delay: a waiting time of about half a period from the last switch must elapse before the system returns to the tracking control mode. A shorter waiting time is imposed for the observer to re-engage, once it was disengaged.

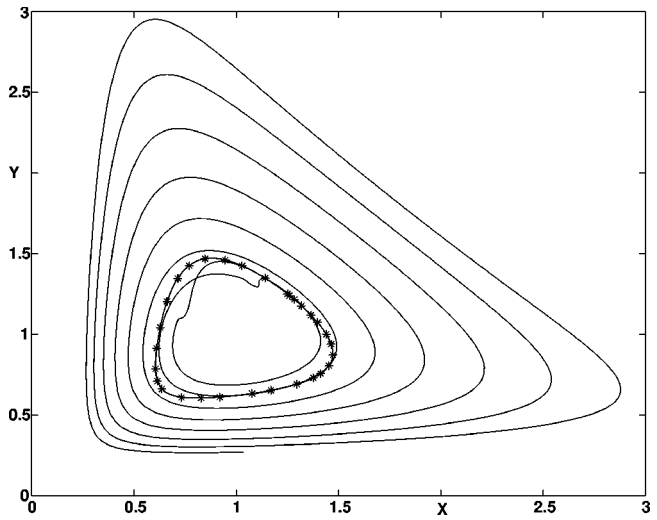

FIG. 25. Closed-loop tracking of a reference vortex orbit. Asterisks, tracking reference orbit; bold, actual vortex trajectory.

Plots of two closed loop trajectories are depicted in Fig. 25. The optimized tracking references have frequency $\Omega=0.5$ and $\Omega=1$. The initial vortex position, in both, is in the far field; it is first driven to closer proximity of the equilibrium point, where the local observer-based tracking controller takes over to produce asymptotic tracking of the reference trajectory.

VIII. CONCLUSIONS AND OUTLOOK

An idealized problem of controlled fluid mixing has been examined which shares important flow features and methodological aspects of realistic applications. One aspect is that the control affects the velocity field but the objectives are specified in terms of particle motion. Enhanced mixing has been achieved in a recirculation zone using a vortex model for the natural and forced dynamics and employing control theory to prescribe the vortex motion. Controllability has been exploited to formulate an optimal mixing problem under suitable side constraints. Thus, the shape of the orbits have been modified by control laws to enhance mixing. The effect of actuation on hydrodynamic mixing has been derived from the invariant manifolds of Poincaré maps at periodic

vortex motion. For instance, the regions of in- and out-going fluid, the fluid exchange across the recirculation region, the region of the trapped fluid, and the residence time distribution have thus been elucidated.

The present study was inspired by the Rom-Kedar, Leonard, and Wiggins[12] investigation of laminar mixing for a vortex pair in free stream with periodic actuation and by studies of Cortelezzi[23,24] on studying control of fluid flows using point vortex methods. It should be noted that the present corner flow configuration is more complicated, since we have to consider four real and mirror vortices in a saddle point potential flow as opposed to only two vortices in simple uniform flow. Hence, part of the investigations cannot be carried out with the same analytical rigor. A main distinguishing feature of the present approach is the application of control theory for actuation. Control theory gives access to a larger class of vortex motion as opposed to periodic forcing employed in the above-mentioned publication.

The present study allows to enhance time-averaged flux by more than 25% as compared to natural vortex motion with same fluctuation amplitude. The higher harmonics in the flat coordinate contribute to the increase of the mixing measure. The size of the mixing region and the flux is approximately proportional to the amplitude of oscillation at constant frequency. The area embraced by the lobes of both invariant manifolds increases strongly with increasing amplitude. Thus, the average residence time decreases with increasing flux. At large amplitudes, a larger portion of fluid particles stays less than one period in the recirculation region. However, the overlap area between both manifolds can be decreased at a nearly constant mixing region with small changes of the frequency. Thus, the flux and the average residence time can to some extent be independently controlled by suitably choosing the desired vortex motion and the corresponding control laws. This possibility represents a clear advantage over the concept of periodic open-loop forcing, in which the frequency difference between the natural and the forcing frequency may lead to quasiperiodic beat phenomena. Periodic vortex motion at non-natural frequencies cannot be excited. The class of controlled vortex motions is significantly larger than the class associated with periodic forcing and thus allows for the specification of different mixing measures.

A potentially interesting consequence of our work is the shape of the optimal flux curve that arises from our optimal mixing setup. Namely, we were able to show that adding a low frequency modulation to periodic vortex motion can increase flux substantially over longer time scales. Thus, the perturbation of the system by control does not have to be on the same (possibly fast) time scale as the natural dynamics of the system in order for control objective to be reached. This coincides with results in several experimental setups that we know of (A. Glezer, private communication). However, the flux is also increased by multiple border-crossings of mixing particles. A conditioned flux measure is suggested which takes into account the identity of the fluid particles.

The fluid dynamics of a recirculation region is highly idealized by the present vortex model. For instance, the shear-layer dynamics at the upper stagnation point has been shown to be of large importance at backward-facing steps[40,41] and in dump combustors,[42] but this effect is neglected in the present study. Similarly, the non-negligible effect of turbulent fluctuations is not considered. Qualitatively, the oscillatory motion of the separating streamline is plausible but the quantitative relationship to a hydrodynamic instability mechanism is not clear. However, experiments of periodically forced flow behind a backward facing step give rise to similar periodic velocity fields. This similarity includes, for instance, the behavior of the instantaneous separating streamline and the motion of the lower separation point.[43] Some observed features of the Lagrangian mixing dynamics can hence be expected to be generic for a large class of recirculation regions. These features include the fluid intake near the separation point at the lower wall, the fluid discharge near the separation point at the vertical wall and the long (ideally infinite) residence time of the fluid trapped around the vortex, neglecting viscous and turbulent diffusion effects. A study of the authors based on a three-dimensional direct numerical simulation and refined vortex models of the backward-facing step confirm similar flow and particle behavior.[29] Hence, several conclusions from the present control study can be expected to qualitatively hold in real flows, e.g., that an increase of the frequency gives rise to a increase of the average residence time.

Numerous generalizations of the present framework may be envisioned and may help to guide industrial applications. Control of coherent shear-layer structures under longitudinal and transverse actuation may be investigated in a similar manner with point vortices or vortex blobs. Present investigations at UTRC[44] indicate that the excitation of certain vortex configurations are beneficial for transversal mixing and pressure recovery in high-Reynolds number diffuser flows. The control of this process requires understanding of vortex merger control, a topic pursued in Ref. 45. Actuation employing control theory for a larger number of vortices might require a re-formulation in the problem: In the Appendix of this paper we show that in order to control trajectories of N vortices, generally N actuating potential fields are necessary. However, control laws need not necessarily depend on a single vortex position, but may be based on properties of an ensemble of vortices, of an ensemble of fluid particles, or of the instantaneous velocity field sensed at one or more locations.[23,24,46] For higher-dimensional vortex methods the receding horizon technique in which a quantity is optimized over a finite period of time, might be employed. In addition, optimization strategies for actuator positions may be carried out in the present framework. Model-based flow control based on Galerkin models, and using control theory with flatness concept is successfully applied to reduce vortex shedding.[47] Current research in this direction is in progress by many authors.

ACKNOWLEDGMENTS

We appreciate valuable stimulating discussions with John Baillieul, Jeff Cohen, Luca Cortelezzi, Andreas Dillmann, Hans-Hermann Fernholz, Ahmed Ghoniem, George Haller, John Hauser, Phil Holmes, Hans-Joachim

Kaltenbach, Alex I. Khibnik, Rudibert King, Satish Narayanan, Anatoly Neishstadt, Mark Pastoor, Bill Proscia, Michael Schlegel, and Tino Weinkauf. This work was supported by the Air Force Office for the Scientific Research Grants Nos. F49620-98-C-0006, F49620-01-C-0021, and F49620-00-1-0361, by the National Science Foundation (NSF) under Grant No. ECS-0136404, and by the Deutsche Forschungsgemeinschaft (DFG) under Grant No. NO 258/1-1. Support of the Collaborative Research Center (Sfb) 557 "Control of Complex Turbulent Shear Flow" funded by the Deutsche Forschungsgemeinschaft and hosted at the Technical University Berlin is acknowledged.

APPENDIX A: GENERALIZATION FOR *N*-VORTEX MOTION AND MORE GENERAL ACTUATION

The considerations given in Sec. III D can be generalized to the case of single vortex motion in an arbitrary domain driven by a potential velocity field with stream function Ψ_a. The equations of motion for the vortex are given by

$$\dot{x}_v = \frac{\partial \Psi}{\partial\, y_v} + a\frac{\partial \Psi_a}{\partial\, y_v},$$

$$\dot{y}_v = -\frac{\partial \Psi}{\partial\, x_v} - a\frac{\partial \Psi_a}{\partial\, x_v}.$$

The stream function of the control field can again be chosen as a flat coordinate, $z_1 = \Psi_a$. The other coordinate, z_2 is chosen such that $\dot{z}_1 = z_2$. Thus,

$$z_2 = \{\Psi_a, \Psi\} = \frac{\partial \Psi_a}{\partial\, x_v}\frac{\partial \Psi}{\partial\, y_v} - \frac{\partial \Psi_a}{\partial\, y_v}\frac{\partial \Psi}{\partial\, x_v},$$

where $\{\Psi_a, \Psi\}$ is the notation for a Poisson bracket of functions Ψ_a, Ψ. The derivative of the second coordinate reads

$$\dot{z}_2 = \{\{\Psi_a, \Psi\}, \Psi\} + a\{\{\Psi_a, \Psi\}, \Psi_a\}.$$

Thus, the motion of a single vortex in a container of arbitrary shape under the influence of a potential field with a stream function Ψ_a is controllable if

$$\{\{\Psi_a, \Psi\}, \Psi_a\} \neq 0 \tag{A1}$$

on the domain. Corresponding dynamics and control laws have also been derived and studied for other local actuations. The actuators are sources (sinks) on the axes. The no-penetration condition is violated only at the actuator position and is enforced elsewhere by mirror sources. The studied actuator configurations include (a) a source at the origin,

$$\Psi_a(\mathbf{x}) = \arctan\left[\frac{y}{x}\right], \tag{A2}$$

(b) a source at positive x axis $(c,0)$ with the corresponding image at $(-c,0)$,

$$\Psi_a(\mathbf{x}) = \arctan\left[\frac{y}{x-c}\right] + \arctan\left[\frac{y}{x+c}\right], \tag{A3}$$

and (c) zero-net flux source-sink combination at $(0,c)$ and $(c,0)$ with corresponding images,

$$\Psi_a(\mathbf{x}) = \arctan\left[\frac{y-c}{x}\right] + \arctan\left[\frac{y+c}{x}\right] + \arctan\left[\frac{x}{y-c}\right] + \arctan\left[\frac{x}{y+c}\right]. \tag{A4}$$

The corresponding analytical expressions for the vortex dynamics and the control laws can become rather long and we shall not pause to discuss them.

Another generalization holds for the case of N vortices under the influence of N potential fields, the stream functions of which are denoted by $\Psi_a^j, j = 1, \ldots, N$. The equations of motion for vortex positions $\mathbf{x}_v^i$, $i = 1,\ldots,N$ are expressed by

$$\dot{x}_v^i = \frac{\partial \Psi}{\partial y_v^i} + \sum_{j=1}^{N} a_j \frac{\partial \Psi_a^j}{\partial y_v^i},$$

$$\dot{y}_v^i = -\frac{\partial \Psi}{\partial x_v^i} - \sum_{j=1}^{N} a_j \frac{\partial \Psi_a^j}{\partial x_v^i}.$$

The Hamiltonian vector field corresponding to Ψ_a^j is called *control vector field*.

In analogy to Eqs. (11) and (12), N coordinates $z_{2i-1}, i = 1, \ldots, N$ have to be found such that

$$\dot{z}_{2i-1} = z_{2i}, \tag{A5a}$$

$$\dot{z}_{2i} = p_i + \sum_{j=1}^{N} a_j q_i^j. \tag{A5b}$$

The time evolution of z_{2i-1} is described by

$$\dot{z}_{2i-1} = \sum_{j=1}^{N} \frac{\partial z_{2i-1}}{\partial x_v^j}\frac{\partial \Psi}{\partial y_v^j} - \frac{\partial z_{2i-1}}{\partial y_v^j}\frac{\partial \Psi}{\partial x_v^j} + \sum_{k=1}^{N} a_k \sum_{j=1}^{N} \frac{\partial z_{2i-1}}{\partial x_v^j}\frac{\partial \Psi_a^k}{\partial y_v^j} - \frac{\partial z_{2i-1}}{\partial y_v^j}\frac{\partial \Psi_a^k}{\partial x_v^j}.$$

Examining the above expression, we conclude that the term multiplying a_k vanishes if we find a function H_i that is an integral of motion for Ψ_a^k. Thus, we can set $z_{2i-1} = H_i$. To have the terms multiplying all a_k vanish, and to bring the system in the required form (A5), N independent functions H_i, $i = 1, \ldots, N$, we must find which are integrals of motion simultaneously for the Hamiltonian vector fields generated by Hamiltonians Ψ_a^k, $k = 1, \ldots, N$. Then, the equations of motion acquire the required form (A5) with $z_{2i-1} = H_i, i = 1, \ldots, n$ and

$$z_{2i} = \sum_{j=1}^{N} \frac{\partial H_i}{\partial\, x_v^j}\frac{\partial \Psi}{\partial\, y_v^j} - \frac{\partial H_i}{\partial\, y_v^j}\frac{\partial \Psi}{\partial\, x_v^j} = \{H_i, \Psi\}.$$

From

$$\dot{z}_{2i} = \{\{H_i, \Psi\}, \Psi\} + \sum_{k=1}^{N} a_k \{\{H_i, \Psi\}, \Psi_a^k\},$$

a sufficient condition for controllability can easily be derived. This condition is a nonvanishing determinant $\det \mathbb{H} \neq 0$ where the components of the matrix $\mathbb{H}$ are given by $\mathbb{H}_{ik} = \{\{H_i, \Psi\}, \Psi_a^k\}$. In the case $N = 1$, this clearly reduces to condition (A1).

The condition on simultaneous integrability of N control vector fields (i.e., the existence of N functions H_i, $i=1,\ldots,N$, which are integrals of motion for each control vector field) seems severe. But, the control vector fields arising in the context of vortex motion are special as it is immediate that they are integrable: the control Hamiltonian Ψ_a^k can be expressed as

$$\Psi_a^k(x_v^1,y_v^1,\ldots,x_v^N,y_v^N)=\sum_{i=1}^{N}\psi^k(x_v^i,y_v^i).$$

Thus, each $\psi^k(x_v^i,y_v^i)$, $i=1,\ldots,N$ is an integral of motion for the control vector field with Hamiltonian Ψ_a^k. It is easy to check that these are also integrals in involution so the control vector fields are integrable Hamiltonian systems. This does not mean that the integrals $\psi^k(x_v^i,y_v^i)$ can be combined in a simple manner to find joint integrals of motion, but makes it easier to search for them in examples.

The conditions obtained here are sufficient for controllability but are not necessary. In general they are too strong, as control terms are used to overwhelm the natural dynamics of vortex motion. Less stringent conditions can be obtained by utilizing natural vortex motion in the control procedure.[45,48]

A general form for arbitrary potential flow control fields Ψ_a is given by $z_1=\Psi_a$, $\dot z_1=z_2=\partial_i(f_i\Psi_a)$, $\dot z_2=p+aq$, where $p=\partial_i[f_i\,\partial_j(f_j\Psi_a)]$ and $q=a_{ij}[\partial_j\Psi_a]\,\partial_i[\partial_k(f_k\Psi_a)]$ using Einstein summation convention, ∂_i for the partial derivative with respect to the ith component of x_v and the antisymmetric tensor $a_{12}=-a_{21}=1$ and $a_{11}=a_{22}=0$. For all considered local actuations, the vortex motion is controllable, i.e., q does not vanish in the domain $x_v,y_v>0$.

APPENDIX B: LOW-FREQUENCY LIMIT OF OPTIMAL VORTEX MOTION

In this appendix, the low-frequency limit of the optimal vortex motion is discussed. To simplify the discussion, we consider a periodic controlled motion which respects all side constraints of the optimization problem, in particular the permissible region $R\leqslant 0.5$ and the actuation bound $A\leqslant 0.5$. The resulting flux thus serves as the lower bound for the optimal vortex motion in Appendix C. Such a controlled motion is, for instance, prescribed by the following flat coordinate:

$$z_1=\left[\frac{43}{48}+\frac{\sqrt{2}}{4}\right]+\left[\frac{11}{48}+\frac{\sqrt{2}}{4}\right]\cos\Omega t. \tag{B1}$$

A straightforward calculation shows $R=A=1/2$ in the limit $\Omega\to 0$. In that limit, the corresponding controlled vortex position moves on the bisector $x=y$ and touches the boundary of the permissible region at $t=0$ and hits the actuation bound $|a|\leqslant 1/2$ at $t=T/2$ where $T=2\pi/\Omega$. The vortex motion is quasisteady, i.e., the position at time t represents the equilibrium point of the steady problem (7) under the frozen actuation $a(t)$ at that instant.

At $t=0$, the vortex is located at $x_v=y_v=1+1/\sqrt{8}$ and the separatrix $\mathcal{C}$, defined by the Poincaré map (20), coincides with the streamline $\Psi=0$, shown in Fig. 26. Obviously, $v=0$ on the positive y axis defines the unstable fixed point $\mathbf{x}_u$ of (20). By symmetry, $u=0$ speficies the stable fixed point $\mathbf{x}_s$ of that map. Both fixed points are connected by the streamline $\Psi=0$. The initial part $\overline{\mathbf{x}_u\mathbf{q}}$, $\overline{\mathbf{x}_s\mathbf{q}}$ of the invariant manifolds are well aligned with $\Psi=0$, since the fluid particles slide from the unstable to the stable fixed point on the $\Psi=0$ curve in the very end of the diverging period in the limit $\Omega\to 0$. Hence, the instantaneous flux through $\mathcal{C}$ vanishes at that instant.

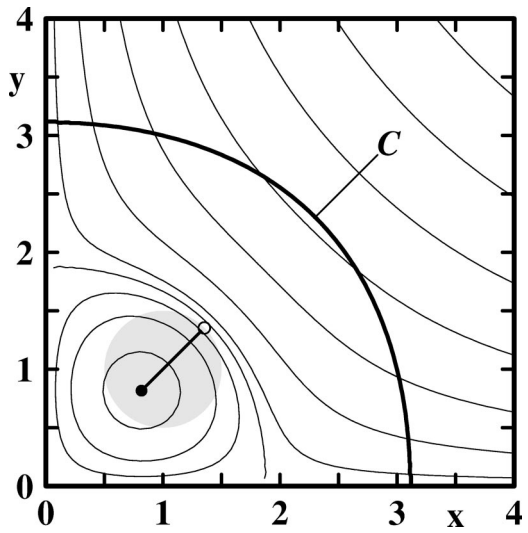

FIG. 26. Low-frequency limit of controlled vortex motion. The flat coordinate is given by (B1). The permissible vortex region is illustrated as a gray circle. The vortex moves on the shown straight bi-sector in the permissible region. The vortex positions at time $t=0$ and $t=T/2$ are indicated by open and solid circles, respectively. The thick circular arc $\mathcal{C}$ represents the recirculuation region as defined by the Poincaré map. The thin curves are streamlines associated with the vortex position at $t=T/2$.

At the opposite phase, $t=T/2$, the vortex is on the opposite side of the orbit, $x_v=y_v=\sqrt{2/3}$. Figure 27 displays the vortex position and the streamlines at time $t=T/2$. The corresponding flow field induces a flux of 6.94 through $\mathcal{C}$. Figure 27 displays the flux as a function of time. In the quasisteady limit $\Omega\to 0$, Q depends on t/T independently of Ω. The averaged flux $\langle Q\rangle$ is 2.86. This value is above the optimal fluxes displayed in Fig. 13 at $0.5<\Omega<1.5$. This value is the lower bound for the optimized flux in the limit $\Omega\to 0$. Hence, the flux in Fig. 13 must increase towards $\Omega=0$.

The numerical computation of the recirculation region with the Poincaré is very difficult at low Ω without simplifying assumptions. The reason lies in the long integration

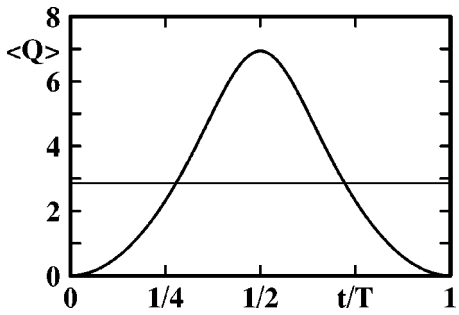

FIG. 27. Instantaneous flux in dependency of the time for the vortex motion of Fig. 26. The thin horizonal line represents the average flux.

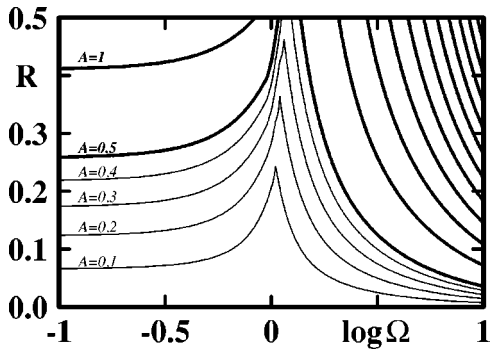

FIG. 28. Actuation amplitude $A(\Omega,R)$ of the controlled vortex motion in dependency of the frequency Ω and the oscillation amplitude R. The flat coordinate is prescribed by (C1). The thin curves show the isolines $A=0.1,0.2,0.3,$ and 0.4. The thick curves represent $A=0.5,1.0,1.5,$ etc.

times and in the large sensitivity of the fluid particle positions on the initial condition near the y axis.

It should be noted that Rom-Kedar and Poje[33] rigorously prove for the large class of perturbed vortex motions that $\langle Q\rangle\to 0$ as $\Omega\to 0$. This class contains their vortex pair in uniform flow perturbed by four far-field vortices. All those vortices are at fixed locations and the circulation of the far-field vortices serves as the control parameter. Thus, the phenomenon of a free-stream-like flux due to a displaced vortex at $t=T/2$ cannot occur in their model. These considerations, including the hypothesized finite flux in the low-frequency limit, suggest that the considered variant of Shu's vortex model does not fulfill all assumptions posed by Rom-Kedar and Poje.[33]

APPENDIX C: HIGH-FREQUENCY LIMIT OF OPTIMAL VORTEX MOTION

In this section, the high-frequency limit of the optimal vortex motion is considered. Focus is placed on the effect of the constraints imposed on the oscillation amplitude R and on the actuation amplitude A. For reasons of simplicity, a controlled motion with the flat coordinate

$$z_1=1+a_1\cos(\Omega t) \tag{C1}$$

is studied. The resulting motion has associated oscillation and actuation amplitudes, R and A, respectively. Figure 28 displays the actuation level as a function of R and Ω. Near the natural oscillation frequency $\Omega\approx 1$, the actuation level is lowest at a given oscillation amplitude. The actuation level does not vanish, since the natural vortex motion does follow the prescribed sinusoidal evolution of the flat coordinate z_1. In the quasisteady limit $\Omega\to 0$, the bound $A=0.5$ gives rise to a finite oscillation amplitude $R\approx 0.25$. The bound $R=0.5$ can be reached by increasing the average value $\langle z_1\rangle$ like in (B1) of Appendix B. In the high-frequency limit $\Omega\to\infty$, the bound $A=0.5$ appears to lead to a vanishing oscillation amplitude R. An approximate analytical study (not shown here) corroborates $R\to 0$ as $\Omega\to\infty$. At constant R, the proportionality $A\propto\Omega$ as $\Omega\to\infty$ can be numerically and analytically corroborated.

Two conclusions can be drawn from this section. First, a flux optimization problem with bounded vortex motion but unbounded actuation does not seem to be well posed. In this case, infinite actuation is achieved with infinite control frequency, e.g., by moving to higher and higher harmonics of the prescribed frequency Ω. As the actuation increases without bound, also the flux through any given curve will increase without bound while the vortex orbit shrinks towards its equilibrium. This ill-posedness of the optimization problem is plausible, but a rigorous analysis would have to include the effect of optimization and the change of the recirculation region with frequency.

A second conclusion is that the bound on the actuation reduces the oscillation amplitude and thus the flux at large Ω (see Fig. 13). In the limit $\Omega\to\infty$, the vortex orbit shrinks around its equilibrium point and the flux is only caused by the finite oscillatory actuation field $a\Psi_a$. In this limit, the time-averaged flux is independent of the oscillation frequency and does not vanish. Again, the nonvanishing flux limit is a plausible hypothesis which is suggested by the present study but which still must be rigorously examined.

Rom-Kedar and Poje[33] rigorously prove that the flux vanishes as $\Omega\to\infty$ for a large class of periodically perturbed vortex motions. Like the low-frequency behavior, also this high-frequency study corroborates that the present motion does not seem to fulfill all of their premises (A1)–(A3).

[1] M. Gad-el Hak, "Modern developments in flow control," Appl. Mech. Rev. **49**, 365 (1996).
[2] M. Gad-el Hak, *Flow Control: Passive, Active and Reactive Flow Management* (Cambridge University Press, Cambridge, 2000).
[3] A. S. Monin and A. M. Yaglom, *Statistical Fluid Mechanics I* (MIT Press, Cambridge, 1971).
[4] A. S. Monin and A. M. Yaglom, *Statistical Fluid Mechanics II* (MIT Press, Cambridge, 1975).
[5] H. Aref, "Stirring by chaotic advection," J. Fluid Mech. **143**, 1 (1984).
[6] J. M. Ottino, *The Kinematics of Mixing: Stretching, Chaos and Transport* (Cambridge University Press, Cambridge, 1989).
[7] G. Haller, *Chaos Near Resonance* (Springer, New York, 1989).
[8] S. Wiggins, *Chaotic Transport in Dynamical Systems* (Springer-Verlag, New York, 1992).
[9] G. Haller and A. C. Poje, "Finite time transport in aperiodic flows," Physica D **119**, 352 (1998).
[10] N. Malhotra, I. Mezić, and S. Wiggins, "Patchiness: A new diagnostic for Lagrangian trajectory analysis in time-dependent fluid flows," Int. J. Bifurcation Chaos Appl. Sci. Eng. **8**, 1053 (1998).
[11] I. Mezić, "Chaotic advection in bounded Navier–Stokes flows," J. Fluid Mech. **431**, 347 (2001).
[12] V. Rom-Kedar, A. Leonard, and S. Wiggins, "An analytical study of transport, mixing and chaos in unsteady vortical flow," J. Fluid Mech. **214**, 347 (1990).
[13] A. C. Poje, G. Haller, and I. Mezić, "The geometry and statistics of mixing in aperiodic flows," Phys. Fluids **11**, 2963 (1999).
[14] P. D. Miller, C. K. R. T. Jones, A. M. Rogerson, and L. J. Pratt, "Quantifying transport in numerically generated velocity fields," Physica D **110**, 105 (1997).
[15] S. Wiggins, "Chaos in the dynamics generated by sequences of maps, with applications to chaotic advection in flows with aperiodic time dependence," Z. Angew. Math. Phys. **50**, 585 (1999).
[16] G. K. Batchelor, *An Introduction to Fluid Dynamics* (Cambridge University Press, Cambridge, 1967).
[17] A. Pentek, T. Tel, and Z. Toroczkai, "Stabilizing chaotic vortex trajectories: An example of high-dimensional control," Phys. Lett. A **224**, 85 (1996).
[18] L. Cortelezzi, K. H. Lee, J. Kim, and J. L. Speyer, "Skin-friction drag reduction via robust reduced-order linear feedback control," Int. J. Comput. Fluid Mech. **11**, 79 (1998).
[19] D. D'Alessandro, M. Dahleh, and I. Mezić, "Control of mixing in fluid

flow: A maximum entropy approach,'' IEEE Trans. Autom. Control **44**, 1852 (1999).
[20]D. V. Treschev, ''The mechanism of destruction of resonance tori of Hamiltonian systems,'' Math. USSR Sbornik **68**, 181 (1991).
[21]B. R. Noack, I. Mezić, and A. Banaszuk, ''Controlling vortex motion and chaotic advection,'' Proceedings of 39th IEEE Conference on Decision and Control 2000, Paper INV 4902, 2000, pp. 1716–1723.
[22]A. Iollo and L. Zannetti, ''Optimal control of a vortex trapped by an airfoil with a cavity,'' Flow, Turbul. Combust. **65**, 417 (2000).
[23]L. Cortelezzi, ''Nonlinear feedback control of the wake past a plate with a suction point on the downstream wall,'' J. Fluid Mech. **327**, 303 (1996).
[24]L. Cortelezzi, Y.-C. Chen, and H.-L. Chang, ''Nonlinear feedback control of the wake past a plate: From a low-order model to a high-order model,'' Phys. Fluids **9**, 2009 (1997).
[25]T. R. Bewley, P. Moin, and R. Temam, ''Optimal and robust approaches for linear and nonlinear regulation problems in fluid mechanics,'' AIAA Paper 97-1872 (1997).
[26]B. Bamieh, I. Mezić, and M. Fardad, ''A framework for destabilization of dynamical systems and mixing enhancement,'' Paper 4980 in Proceedings of the 40th IEEE Conference on Decision and Control, 2001.
[27]O. M. Aamo, M. Krstić, and T. R. Bewley, ''Fluid mixing by feedback in Poiseuille flow,'' Proceedings of the 2001 American Control Conference, 2001.
[28]Y. K. Shu, ''Periodic motion of a point vortex in a corner subject to a potential flow,'' J. Phys. Soc. Jpn. **62**, 3441 (1993).
[29]M. Pastoor, R. King, B. R. Noack, A. Dillmann, and G. Tadmor, ''Model-based coherent-structure control of turbulent shear flows using low-dimensional vortex models,'' AIAA Paper 2003-4261, 33rd AIAA Fluids Conference and Exhibit, 2003.
[30]V. I. Arnold, V. V. Kozlov, and A. I. Neishtadt, *Mathematical Aspects of Classical and Celestial Mechanics* (Springer-Verlag, Berlin, 1988), Theorem and Remark after Theorem 17, Chap. 5, Sec. 3.3.
[31]H. Nijmeijer and A. J. van der Schaft, *Nonlinear Dynamical Control Systems* (Springer-Verlag, New York, 1990).
[32]M. Fliess, J. Lévine, P. Martin, and P. Rouchon, ''On differentially flat nonlinear systems,'' in *Nonlinear Control System Designs*, edited by M. Fliess (Pergamon, New York, 1992), pp. 408–412.
[33]V. Rom-Kedar and A. C. Poje, ''Universal properties of chaotic transport in the presence of diffusion,'' Phys. Fluids **11**, 2044 (1999).
[34]J. Guckenheimer and P. Holmes, *Nonlinear Oscillations, Dynamical Systems, and Bifurcation of Vector Fields* (Springer-Verlag, New York, 1986).
[35]W. H. Press, B. P. Flamery, S. A. Teukolsky, and W. T. Vetterling, *Numerical Recipes, The Art of Scientific Computing* (Cambridge University Press, Cambridge, 1986).
[36]T. Takigawa, N. Ohmura, K. Yagyuu, and K. Kataoka, ''Information complexity of laminar chaotic mixing field produced by two parallel, rotating cylinders,'' Forma **15**, 273 (2000).
[37]G. Tadmor and A. Banaszuk, ''Observer based control of vortex motion in a combuster recirculation region,'' in *Nonlinear Control Systems 2001*, edited by A. B. Kurzhanski and A. L. Fradkov (Elsevier, Amsterdam, 2002), pp. 1315–1318.
[38]G. Tadmor and A. Banaszuk, ''Observation feedback control of vortex motion in a recirculation region,'' IEEE Trans. Control Syst. Technol. **10**, 749 (2002).
[39]C. L. DeMarco and G. C. Verghese, ''Bringing phasor dynamics into the power system load flow,'' *Proceedings of the 25th North American Power Symposium* (IEEE Power Engineering Society, 1993), pp. 463–469.
[40]K. R. McManus, U. Vandsburger, and C. T. Bowman, ''Combustor performance enhancement through direct shear layer excitation,'' Combust. Flame **82**, 75 (1990).
[41]D. Wee, S. Park, R. Miake-Lye, A. M. Annaswamy, and A. F. Ghoniem, ''Reduced-order modeling of reacting shear layer,'' AIAA Paper 2002-0478 (2002).
[42]H. N. Najm and A. F. Ghoniem, ''Numerical simulation of the convective instability in a dump combustor,'' AIAA J. **29**, 911 (1991).
[43]J. M. Cohen, ''Transient flow over a backward-facing step,'' Ph.D. thesis, The University of Connecticut, 1995.
[44]S. Narayanan, B. R. Noack, A. Banaszuk, and A. I. Khibnik, ''Dynamic separation control in 2D diffuser,'' Technical Report 1.910.9901-4.1, United Technologies Research Center, 1999.
[45]D. Vainchtein and I. Mezić, ''Control of a vortex pair using a weak external flow,'' J. Turbulence **3**, 1 (2002).
[46]L. Cortelezzi, A. Leonard, and J. C. Doyle, ''An example of active circulation control of the unsteady separated flow past a semi-infinite plate,'' J. Fluid Mech. **260**, 127 (1994).
[47]J. Gerhard, M. Pastoor, R. King, B. R. Noack, A. Dillmann, M. Morzyński, and G. Tadmor, ''Model-based control of vortex shedding using low-dimensional Galerkin models,'' AIAA Paper 2003-4262, 33rd AIAA Fluids Conference and Exhibit, 2003.
[48]I. Mezić, ''Controllability, integrability, and ergodicity,'' *Proceedings of the Mohammed Dahleh Symposium, Santa Barbara, CA 93105* (Springer-Verlag, New York, 2003).